



저작자표시-비영리-변경금지 2.0 대한민국

이용자는 아래의 조건을 따르는 경우에 한하여 자유롭게

- 이 저작물을 복제, 배포, 전송, 전시, 공연 및 방송할 수 있습니다.

다음과 같은 조건을 따라야 합니다:



저작자표시. 귀하는 원저작자를 표시하여야 합니다.



비영리. 귀하는 이 저작물을 영리 목적으로 이용할 수 없습니다.



변경금지. 귀하는 이 저작물을 개작, 변형 또는 가공할 수 없습니다.

- 귀하는, 이 저작물의 재이용이나 배포의 경우, 이 저작물에 적용된 이용허락조건을 명확하게 나타내어야 합니다.
- 저작권자로부터 별도의 허가를 받으면 이러한 조건들은 적용되지 않습니다.

저작권법에 따른 이용자의 권리는 위의 내용에 의하여 영향을 받지 않습니다.

이것은 [이용허락규약\(Legal Code\)](#)을 이해하기 쉽게 요약한 것입니다.

[Disclaimer](#)

공학박사학위논문

아노다이징의 국부화 기술을 이용한
마이크로 산화알루미늄 패턴 가공

Micro Fabrication of Aluminum Oxide Patterns using
Local Anodization

2015 년 8 월

서울대학교 대학원

기계항공공학부

지 원 영

아노다이징의 국부화 기술을 이용한 마이크로 산화알루미늄 패턴 가공

Micro Fabrication of Aluminum Oxide Patterns using
Local Anodization

지도교수 주 종 남

이 논문을 공학박사 학위논문으로 제출함

2015년 4월

서울대학교 대학원

기계항공공학부

지 원 영

지원영의 공학박사 학위논문을 인준함

2015년 6월

위원장 : 이 정 훈 

부위원장 : 주 종 남 

위원 : 안 성 훈 

위원 : 차 석 원 

위원 : 김 보 현 

**Micro Fabrication of Aluminum Oxide Patterns using
Local Anodization**

DISSERTATION

SUBMITTED TO THE SCHOOL OF MECHANICAL
AND AEROSPACE ENGINEERING AND THE COMMITTEE ON
GRADUATE STUDIES OF SEOUL NATIONAL UNIVERSITY
IN PARTIAL FULFILLMENT OF THE REQUIREMENTS
FOR THE DEGREE OF DOCTOR OF PHILOSOPHY

Won Young Jee

August 2015

Abstract

Won Young Jee

School of Mechanical and Aerospace Engineering

The Graduate School

Seoul National University

In this study, the fabrication process of aluminum oxide pattern using local anodization was investigated. This process is known as local anodic oxidation (LAO) or scanning probe microscope (SPM) lithography for nano scale surface texturing [1]. However, an aluminum oxide formed by SPM anodization process has the ultimate thickness (the order of several tens of nm). Electrochemical machining (ECM), based on the electrochemical reactions between two electrodes, is a method for the machining of conductive materials. Micro ECM that uses ultra-short pulses allows localization of the electrochemical reaction to only a few micrometers of the surface due to the selective charging of a double layer. Therefore, using a principle of micro ECM, the aluminum oxide with micro scale depth can be

localized. In the present study, mixtures of sulfuric/oxalic acid electrolyte was tested as feasible electrolytes for aluminum. Behavior of localized oxide growth was analyzed using by field emission scanning electron microscopy (FE-SEM) including energy dispersive spectroscopy (EDS) and it was confirmed that the number of micro-depth localized aluminum oxide was fabricated at specific location on aluminum surface. Depth and width of the anodized oxide line were investigated in different ratios of sulfuric and oxalic acid mixtures at various microsecond pulse duration and applied voltage condition. The insulation characteristics of fabricated aluminum oxide line were investigated and verified its possibility as an electric circuit. Subsequently, a coplanar waveguide (CPW) micro patch antenna was fabricated and characterized by a PNA network analyzer. The local anodization can be used for fabricating micro-electric circuits without masks and substrate; which will promise the next generation of micro electronic devices.

Keywords: Local anodization, Local anodic oxidation, Scanning probe microscope lithography, Micro electrochemical machining, aluminum oxide, RF antenna

Student number: 2008-22894

Contents

Abstract.....	i
Contents	iii
List of Figures.....	v
List of Tables	ix
1. Introduction.....	1
1.1 Research background	1
1.2 Research objective and dissertation overview	4
2. Principle and experiments.....	6
2.1 Principle of local anodization	6
2.1.1 The Mott-Cabrera model.....	7
2.1.2 Chemical reaction	12
2.1.3 Oxide growth of typical anodization	17
2.1.4 Electrochemical with short pulses.....	20
2.2 Experimental system	25
2.2.1 Positioning system	28

2.2.2 Pulse generator	30
2.2.3 Fabrication of tool electrode.....	32
3. Characteristics in local anodization	34
3.1 Oxide growth	29
3.2 Gap between tool electrode and workpiece	51
3.3 Ratio and concentration of electrolyte	56
3.4 Pulse conditions	64
4. Fabrication of aluminum oxide pattern and application	70
4.1 Fabrication of aluminum oxide pattern	70
4.1.1 Local anodization conditions.....	70
4.1.2 Fabrication of aluminum oxide pattern	72
4.2 Fabrication of radio-frequency antenna	78
2.2.1 Introduction of RF patch antenna	78
2.2.2 Fabrication of coplanar waveguide patch antenna	81
2.2.3 Local anodization on the non-flat aluminum surface	92
5. conclusion	97
Reference	99

List of Figures

Fig. 2.1 The interface of the adjacent to the barrier layer [34].

Fig. 2.2 Current-time curve and schematic for a typical anodization

Fig. 2.3 Double layer model[37]

Fig. 2.4 Difference of charging potentials [37]

Fig. 2. 5 Difference of charging potentials

Fig. 2.6 Schematic diagram of experimental system

Fig. 2.7 Schematic diagram of WEDM for fabrication of micro electrode

Fig. 2.8 Fabricated tool electrodes: (a) schematic of tool electrode,

(b) fabricated ϕ 40 μm tool electrode

Fig. 3.1 Aluminum oxide formed by local anodization: (a) SEM image of aluminum oxide, top view, (b) 2D surface profile of section a-a'

Fig. 3.2 3D surface profile of the localized aluminum oxide

Fig. 3.3 SEM image of the cross section of localized aluminum oxide formed by local anodization

Fig. 3.4 Analysis of the cross section of aluminum oxide: (a) Target space of the EDS analysis (b) EDS map data of the surface

Fig. 3.5 EDS profile of the cross section of aluminum oxide

Fig. 3.6 FE-SEM images of the cross section of center of the oxide

Fig. 3.7 The height of the oxide according to time

Fig. 3. 8 FE-SEM images of a cross section and surface of localized aluminum oxide (etched by FIB)

Fig. 3. 9 FE-SEM image of a cross section of a porous oxide layer

Fig. 3. 10 BSE micrographs of cross section and dense oxide layer [42]

Fig. 3. 11 Load-depth curves of localized oxide by nano indentation test

Fig. 3. 12 SEM image of oxide 15 μ m inter-electrode gap at 20 V

Fig. 3. 13 Simulation results of Φ_c according to distance

Fig. 3. 14 Localized oxide surface according to time (a) 5 μ m gap, (b) 10 μ m gap

Fig. 3.15 SEM image of the local anodization in 0.1 M H₂SO₄ electrolyte

Fig. 3.16 Anodized aluminum oxide line in different concentration of electrolyte (a) 0.1 M H₂SO₄, 20 V (b) 1 M H₂SO₄, 10 V

Fig. 3.17 Depth and width of the anodized oxide in different ratio of H₂SO₄/C₂H₂O₄ acid mixtures

Fig. 3. 18 SEM images of cross section of the oxide line at 25 V (a) C₂H₂O₄ (b) C₂H₂O₄ + H₂SO₄ = 1:1 (c) 0.5 M H₂SO₄

Fig. 3.19 Pulse signal

Fig. 3.20 Depth and width of the anodized oxide in different pulse on-time

Fig. 3.21 Charging voltage according to pulse on-time

Fig.4.1 Exposure time of the point on the path line

Fig. 4.2 Micro oxide pattern by local anodization (\varnothing 40 μm electrode, 500 μm thick Al sheet, 20 V, 500 ns pulse on-time, 5 μs period)

Fig. 4.3 SEM images of the fabricated penetrating oxide line (top, bottom)

Fig. 4.4 Optical image of penetrating oxide line by local anodization

Fig.4.5 SEM images of aluminum oxide pattern. (a) top view

Fig. 4.6 Basic features of a patch and CPW patch antenna

Fig.4.7 The geometrical configuration of the CPW micro patch antenna on aluminum sheet.

Fig.4.8 The fabricated CPW patch antenna using local anodization and was attached on the SMA connector.

Fig.4.9 The absorbing performance of the fabricated CPW patch antenna

Fig.4. 10 The geometrical configurations of air-backed antenna and antenna on polyimide substrate

Fig.4. 11 The fabricated CPW patch antenna with polyimide substrates by LBM and was attached on the SMA connector

Fig.4. 12 Comparison of performance with reflection loss (S_{11}) and bandwidth (-10 dB)

Fig.4.13 Local anodization process on the curved surface

Fig.4.14 Schematic of the rotation system for local anodization on curved surface and image of fabrication

Fig.4.15 Optical and SEM image of aluminum oxide pattern on non-flat surface

List of Tables

Table 2.1 Specification of positioning system

Table 2.2 Specifications of the pulse generator

Table 3.1 Conditions of local anodization

Table 3. 2 Conditions and results of the nano-indentation

Table 3.3 EDS analysis of area 1, 2 in Fi. 3.8 (b)

Table 3.4 Conditions of local anodization

Table 4.1 Conditions of local anodization for penetrating oxide line

Table 4. 2 Conditions of laser beam machining process

Table 4.3 Conditions of local anodization for oxide pattern on curved surface

Chapter1

Introduction

1.1 Research background

Anodic oxidation or anodizing is an electrolytic process for producing thick oxide coatings that can improve physical and chemical properties for application of aluminum [2]. The anodic oxide coating also provide abrasion resistance, an electrical insulation, and absorbing dyestuffs to give a wide range of colors [1, 3]. Therefore, anodic oxide films on aluminum have been investigated for improving its electrical/chemical corrosion resistance and decorative coating [4-6]. Many studies show that various electrolyte of acid or acid mixtures can be used for their purposes. The most widely used anodizing specification is a U.S. military spec. MIL-A-9625, which defines three types of aluminum anodization. (Type I -

chromic acid, Type II & III- sulfuric acid) [7]. Other electrolytes are organic acid (such as oxalic acid, malic acid, etc.), phosphoric acid, and so on [1, 2].

As the market demands changes that require micro technologies in electronics industry and electrical circuits became extremely compact,[8] various attempts have been made to use dielectric characteristics of anodic aluminum oxide in the fabrication of micro-electric components and micro-engineered structures. Kikuchi et al. introduced electrochemical etching/deposition techniques with the combination of anodizing and laser irradiation [9-11]. Aluminum specimens covered with porous type anodic oxide films were irradiated with a pulsed Nd-YAG laser to remove the oxide films locally, and then electrochemical etching or deposition were carried out on the exposed local aluminum surface. In their studies, aluminum oxide films were used for electrochemical etching/deposition mask, and were removed after the process.

The self-organized nanopore structures have also attracted attention due to their high pore density and their potential use for masking or micro sensors for electronic industry [12-15]. In the present studies, self-organized hexagonal arrays of uniform parallel nanopores (Anodic Aluminum Oxide, AAO) was used for various

applications in the fields of sensing, storage, separation, and the synthesis of one-dimensional nanostructures [16-19].

The concept of local anodization began with scanning probe microscopes (SPM) or atomic force microscope (AFM) [20, 21]. There have been many reports on the use of this technique to produce nanoscale patterns and transfer them into underlying material. In this technique, a voltage is applied between the conductive tip and the material's surface, resulting in the formation of a narrow oxide line along the path followed or dot array by the advantage of precise control of local insulator fabrication. Meanwhile, an aluminum oxide formed by SPM anodization process has the ultimate thickness, the order of several tens of nm. If the thickness of oxide films are increased to micro scale, local aluminum oxide can be used for dielectric material of hard-to-make micro devices. In GHz radio frequency antenna engineering, for example, helical antenna structures that have high performance (bandwidth radiation efficiency, radiation resistance and optical transmission coefficient) than 2D structures are difficult to make [22]. The LIGA process, the most commonly used to make micro patch antenna, is limited to the fabrication of 2D micro structures with high aspect ratio [23-27]. Micro milling, micro EDM (electrical discharge machining), micro ECM (electrochemical machining) and LBM (laser beam machining) can be applied to machine micro structures with high

precision. However, these are all cutting process thus micro helical structure of antenna materials like copper or aluminum have robustness problem with maintaining its shape. Unfortunately, any other dielectric substance than air inside the helical structure to support decrease the antenna performance [22].

In this case, local anodization can be applied. Penetrating localized oxide of aluminum sheet may acts a dielectric space of helical strip and support the entire structure. Park et al. propose the local anodization process with photoresist mask patterns on aluminum surface to fabricate localized alumina line [28]. Yet, there is also a limitation on applying at non-flat surface. To apply the local anodization technique to micro manufacturing, further studies on increasing the depth of localized oxide on flat and non-flat surfaces are required.

1.2 Research objective and dissertation overview

In this dissertation, by using a principle of micro ECM, local anodization process to form the aluminum oxide with micro scale depth was investigated. Mixtures of sulfuric/oxalic acid electrolyte was tested as feasible electrolytes for aluminum. Behavior of localized oxide growth was analyzed using by field emission scanning

electron microscopy (FE-SEM) including energy dispersive spectroscopy (EDS) and it was confirmed that the number of micro-depth localized aluminum oxide was fabricated at specific location on aluminum surface. Depth and width of the anodized oxide line were investigated in different ratios of 0.5 M sulfuric and 0.5 M oxalic acid mixtures at various microsecond pulse duration and applied voltage condition. The insulation characteristics of fabricated aluminum oxide line were investigated and application of local anodization is also introduced.

In chapter 2, the principal of local anodizing based on the Mott-Cabrera model and chemical reaction are presented. Description of experimental system is also presented.

In chapter 3, the oxide growth and the characteristics of the local anodization are presented. The effects of electrolytes, pulse conditions, and gap between tool and workpiece are analyzed.

In chapter 4, the fabrication of aluminum oxide pattern and micro patch antenna by local anodization is presented. The performance of the fabricated patch antenna was measured. Furthermore, local anodization is applied to non-flat cylindrical surface. As a result, possibility of using on fabrication of 3D micro electric circuit

Conclusion of this dissertation and discussion were presented in chapter 5.

Chapter 2

Principle and experiments

2.1 Principle of local anodization

Since the initial demonstration of surface anodization of semiconductors with SPM or AFM technology [21], there have been many reports about the physical mechanism and its relevance to anodization thickness and linewidth [20]. Actually, the oxide growth on metal surface starts out quickly but virtually stops after an oxide of finite thickness has been formed. The formation of this native oxide can be explained within the framework of the theory originally developed by Nevill Mott and Nicolas Cabrera [29, 30]. The additional oxide thickness can be attributed to the field assisted Mott-Cabrera mechanism [31]. Although this theory explains the nano-scale phenomenon, it will be reasonable to understand mechanism of local anodization.

2.1.1 The Mott-Cabrera model

This model is discussed by follow the usual conventions[31, 32] and assume a quasi-one-dimensional system consisting of:

1. The parent material, *i.e.*, bulk metal or semiconductor, for $x \in (-\infty, 0)$
2. An oxide layer of thickness X in the region $x \in (0, X)$
3. A source of oxygen, *e.g.*, air or water, for $x \in (X, \infty)$

After the formation of initial oxide layer, ions or ionic defects or neutral atoms should be transported through this film. In the steady state approximation, the concentration n_s of each diffusing species s is assumed to be constant in time. Particle conservation, in the form of the continuity equation $\partial n_s / \partial t = \partial j_s / \partial x$, then dictates that $\partial j_s / \partial x = 0$ and the particle current j_s is constant throughout the oxide. Accordingly, the oxide growth rate can be wrote as

$$\frac{dX}{dt} = \sum_s \Omega_s j_s \quad (2.1)$$

where Ω_s is the volume of oxide formed by the transversal of a single ion of species s [32].

In general, the growth of oxide films is controlled by diffusion of ions and electrons under the influence of gradients of their concentrations and self-generated electric potential.: The contribution V_ρ to the potential due to the space charge $\rho(x) = \sum_s q_s n_s(x)$, where q_s is the charge of a single ion of species s , can be found from Poisson's equation and evaluates to $(1/2\epsilon)X^2\rho$ if ρ is independent of x ; if $X \ll \sqrt{\epsilon k_B/e\rho}$, eV_ρ is small compared with $k_B T$. [31].

By mott-cabrera assumption, electrons are transported through thin oxide films via tunneling or thermal emission and the electronic motion is rapid compared to the ionic motion. If a layer of oxygen is present at X , some of the oxygen atoms will be converted to O^- ions until the chemical potential is equal on both sides of the oxide. This charge separation causes a built-in voltage V_M across the oxide, which is sometimes designated the Mott potential [31]. The magnitude of V_M may be estimated by $eV_M \approx EA_O + W - \varphi_m$, where EA_O is the electron affinity of oxygen, W the binding energy of the oxygen ion, and φ_m the work function of the parent material; V_M is typically of the order 1V.

For thin films, the electric field $E = V_M/X$ becomes large and controls the ionic transport. If the particle current j_s of ions of species s obeys the linear relation

$j_s = \mu_s E$, where μ_s is the mobility, the assumption of single carrier transport leads to a growth rate [31, 32]

$$\frac{dX}{dt} = \frac{\Omega \mu V_M}{X} \quad (2.2)$$

which can be integrated to give the well-known parabolic law [29, 30]

$$X(t) \propto \sqrt{t - t_0} \quad (2.3)$$

with constant of proportionality $\sqrt{2\Omega\mu V_M}$.

For very thin oxide layers, however, the electric field becomes so strong that j_s is no longer proportional to E . In this case, the relationship between the electric field and the particle current can be derived from the hopping model originally formulated by Verwey [30, 33]: Let the distance between adjacent potential minima in the oxide be a and the energy barrier between them U . The classical Boltzmann probability that a particle will move from one site to the next is then $\nu \exp(-\frac{U}{k_B T})$, where the attempt frequency ν can be identified with the typical phonon frequency [30, 33]. An electric field $E(x)$ lowers the activation energy barrier for movement in the positive x -direction by $\frac{1}{2} a q_s E(x)$. The hopping probability thus becomes $\nu \exp[-\{U - \frac{1}{2} a q_s E(x)\}/k_B T]$ in the forward direction, while the probability for

hopping in the reverse direction is reduced to $\nu \exp\left[-\left\{U + \frac{1}{2}aq_sE(x)\right\}/k_B T\right]$ and can be neglected in the strong field limit $aq_sE(x) \gg k_B T$. The particle current of species s is therefore given by

$$j_s \approx \frac{n_s(x)}{a} \nu \exp\left(\frac{-U}{k_B T}\right) 2 \sinh\left[\frac{\frac{1}{2}aq_sE(x)}{k_B T}\right]. \quad (2.4)$$

In the strong field limit, $\frac{1}{2}aq_sE(x) \gg k_B T$ and $2 \sinh\left[\frac{\frac{1}{2}aq_sE(x)}{k_B T}\right]$ can be approximated by $\exp\left[\frac{\frac{1}{2}aq_sE(x)}{k_B T}\right]$. Assuming that space charges are negligible, $E(x) = V_M/X$, $n_s(x) = n_s(0)$ and Eq. (2.4) becomes

$$j_s \approx \frac{n_s(0)}{a} \nu \exp\left(\frac{-U}{k_B T}\right) \exp\left[\frac{\frac{1}{2}aq_s V_M}{k_B T X}\right] \quad (2.5)$$

For single carrier transport, Eqs. (2.1) and (2.5) imply

$$\frac{dX}{dt} \approx \Omega \frac{n(0)}{a} \nu \exp\left(\frac{-U}{k_B T}\right) \exp\left[\frac{\frac{1}{2}aq V_M}{k_B T X}\right] \quad (2.6)$$

If transport through the oxide is rate determining, $n(0)$ is approximately independent of the oxide film thickness and determined by interfacial equilibrium conditions [33]. In contrast, if we follow Mott and Cabrera in assuming that the

transport in the presence of a strong field is very rapid and the limiting step is the dissolution of the ions at the interface, the rate of oxidation is given by

$$\frac{dX}{dt} \approx \Omega N' \nu \exp\left(-\frac{W_i+U}{k_B T}\right) \exp\left[\frac{1}{2} \frac{aq}{k_B T} \frac{V_M}{X}\right] \quad (2.7)$$

Where W_i is the heat of solution of the ion, b the width of the energetic barrier it has to overcome, and N' is the sheet density of ions available for dissolution [30].

The derivation is analogous to the argument given above.

In both cases, dX/dt has the same functional form

$$\frac{dX}{dt} = u_0 \exp\left(\frac{-W}{k_B T}\right) \left(\frac{X_0}{X}\right) \quad (2.8)$$

By considering growth to have stopped once $dX/dt \gtrsim u_L$, a limiting oxide thickness X_L can be defined as

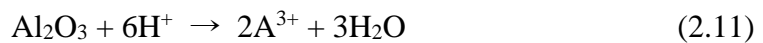
$$X_L = \frac{X_0}{W/k_B T - \ln(u_0/u_L)} \quad (2.9)$$

Following this conclusion, the oxide growth will stop at a thickness $X_L \propto X_0 \propto V_M$ provided that $W/[k_B T - \ln(u_0/u_L)]$, in agreement with the observed behavior of many metals [30].

The Mott–Cabrera-model is also applicable to the anodic formation of oxide films in an electrolyte [30] and LAO was originally explained as a straightforward extension to it. In the vicinity of the probe, the applied bias would lead to a larger voltage V dropped across the oxide. The oxide growth would terminate at a larger final oxide thickness X_L in the affected areas [21].

2.1.2 Chemical reaction

The two main reactions of the formation of the porous oxide layer are (2.10) and (2.11). Reaction (2.10) shows the formation of aluminum oxide and reaction (2.11) the chemical dissolution of the oxide layer in an acidic electrolyte, such as sulfuric acid.



Beside reaction (2.11), another dissolution process must exist. When the rate of oxide growth is almost twice as high for a current, the chemical dissolution should double as it should to keep a steady state for formation and dissolution. This process is called the field-assisted dissolution. The field-assisted dissolution is a result of concentration of the field across the barrier layer. It causes concentration of the

current and thermally enhanced through local Joule's heating [1]. This thermal energy weakens the Al-O bonds in the oxide lattice and causes a dissolution at the film/electrolyte interface. Between these two dissolution mechanisms, the chemical dissolution is much slower than the field-assisted dissolution [1].

The most important factor in aluminum anodizing is the behavior of the barrier layer. The electrical field across the barrier layer controls the dissolution rate of the oxide layer. In this regard, reaction (2.10) is a purely field-assisted process. The electrical field is the main reason for the possibility of the ions to move through the barrier layer at all. Many considerations have been done to explain this formation process of aluminum oxide.

Aluminum has the face centered cubic (fcc) crystal lattice. When Al^{3+} ions leave this metal lattice, vacancies are formed. These vacancies provide room for the ingress of oxygen ions from the adjacent oxide layer to continue the formation of aluminum oxide. Due to the very small radius of Al^{3+} , the ion can diffuse through the barrier layer under the influence of the electrical field easily present. The continued growth of the film is possible which makes the radius of Al^{3+} is 0.5 \AA and that of O^{2-} is in the order of 1.3 \AA . The size of the oxygen ions makes the movement of these ions possible only when there is sufficient space. Hoar and Mott⁹ suggested that the oxygen is transported not as O^{2-} but as OH^- which is much

smaller. The H^+ ions found in the electrolyte may lead to the production of a hydroxyl ion instead of the oxygen ion according to reaction (2.12).



Under the influence of the high field, the hydroxide ions will move through the oxide to the interface metal/barrier layer. It will react with Al^{3+} , which is formed here and form aluminum oxide. If the oxide is formed by the hydroxide rather than the oxygen ions positive hydrogen ions will move back through the film and into the electrolyte. This means that the continuous formation of oxide (2.10) is dependent on the ability of migration of aluminum and oxygen ions through the barrier layer as shown in Fig. 2.1. Takahashi et al. [34] show the migration of oxygen ions through the barrier layer into the interface area metal/barrier layer where the reaction takes place. They do not take into considerations if the oxygen ion is too big to migrate through the aluminum oxide lattice. They also postulate that chemical dissolution, reaction (2.11), will take place at the interface barrier layer/electrolyte at a rate keeping the thickness of the barrier layer constant as determined by the applied voltage [34].

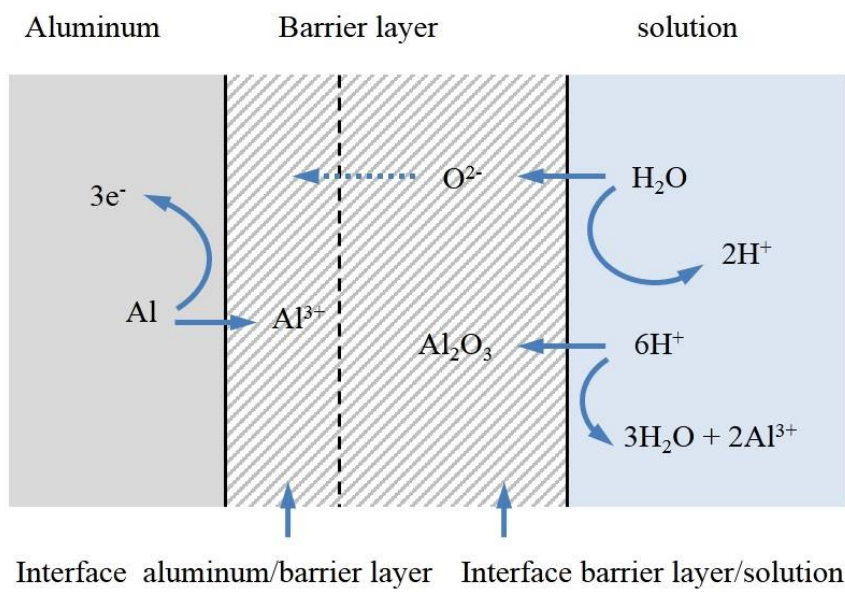


Fig. 2.1 The interface of the adjacent to the barrier layer [34].

2.1.3 Oxide growth of typical anodization

Investigations by a group at UMIST [1] give an explanation of the formation of porous oxide. They conclude that in all cases of film growth examined, Al^{3+} and O_2^-/OH^- are mobile; the latter always develops solid film at the interface between metal and film whereas the contribution of outwardly mobile Al^{3+} ions to film formation depends upon the specific conditions of anodic polarization.

The initial stages of oxide growth correspond to a relatively uniform oxide thickness but by the egress of aluminum ions into the electrolyte penetration paths will develop in top of the barrier layer. Between these penetration paths there will be a decrease in field strength and hence a decrease in the field assisted dissolution rate. As a consequence of these variations in the field strength the interface of aluminum and barrier layer will adopt the form of a fine scalloped structure. By concentration in the barrier layer of the electric field and the ionic current, beneath the major pores, a steady state porous anodic film is formed. The current - time curve obtained during the first 100 seconds of the anodizing will be as shown in Fig. 2.2. Here the process is performed with constant voltage during the anodizing process.

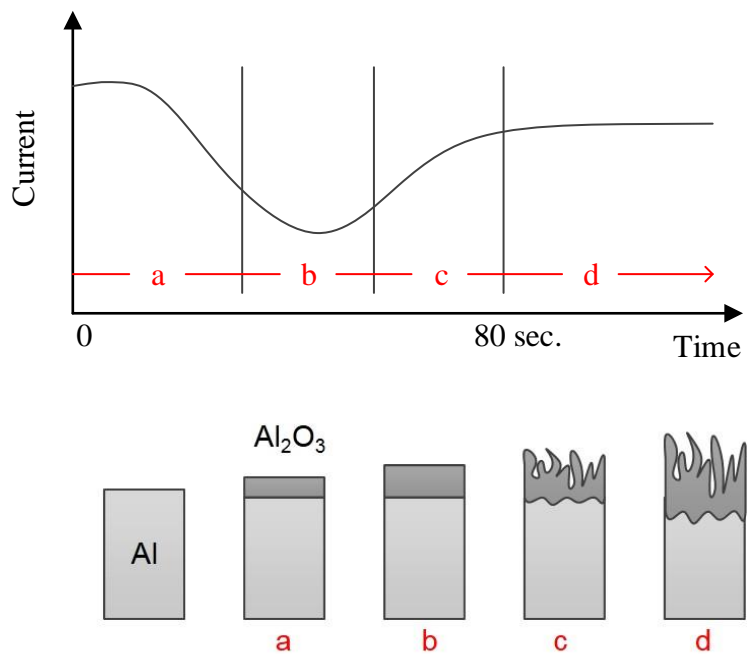


Fig. 2.2 Current-time curve and schematic for a typical anodization

Period a in Fig. 2.2 shows the formation of the first microns of oxide. In the beginning the current is high due to the fact that the current only passes through the metallic aluminum. Then the current starts to decrease because of the formation of a thin non-porous oxide layer. This oxide layer has a higher resistance than the metallic aluminum. The increase in thickness and therefore an increasing resistance result in a further decrease in the current in period b. The tendency of the curve to turn upwards in period b is due to small imperfections (roughness) in the compact oxide layer. These small imperfections are formed by the concentration of the current in areas with thinner oxide than on the rest of the surface. According to Keller et al. [35] these areas with the small imperfection are the subgrain boundaries found on aluminum. They stated that these areas are the places where the initial formation of cells starts. The natural oxide film on either side of these subgrain boundaries is not as compact or uniform as on the rest of the surface. Therefore these areas offer less resistance to the current. Considering the formation of a single cell of oxide. At a single point the dissolution reaction is started, hence the oxide thickness is reduced and the current will start to flow to repair the damage. This will increase the temperature of the electrolyte and the solution will be more reactive and thus increase the rate of dissolution. This mechanism will perpetuate a

pore once formed. According to Keller et al. [35] this mechanism could be halted. Therefore some pores will perpetuate and others will never get started. Hence the current will concentrate on these small imperfections. This will increase the electrolyte temperature in these areas. Therefore the dissolution will increase and the oxide layer will become even thinner. The current will increase as seen in period c in Fig 2.2. Now the formation of the porous oxide layer has started. In period d the current will reach a constant level where the rates of dissolution and formation of the oxide layer reach a steady state level.

2.1.4 Electrochemical cell with short pulses

During the anodization, when the initial oxide layer (barrier layer) has formed, enough mass cannot pass through the layer for the continuous oxide growth. To form thick oxide layer, increase the rate of field-assisted dissolution through barrier layer using high voltage. Therefore, high and local electrical field should be restricted to the target region to localize the oxide. Localized anodizing uses principle of micro ECM, which uses very close to the electrode end to workpiece and localize the electrochemical reaction region by the ultra-short pulse voltage [36].

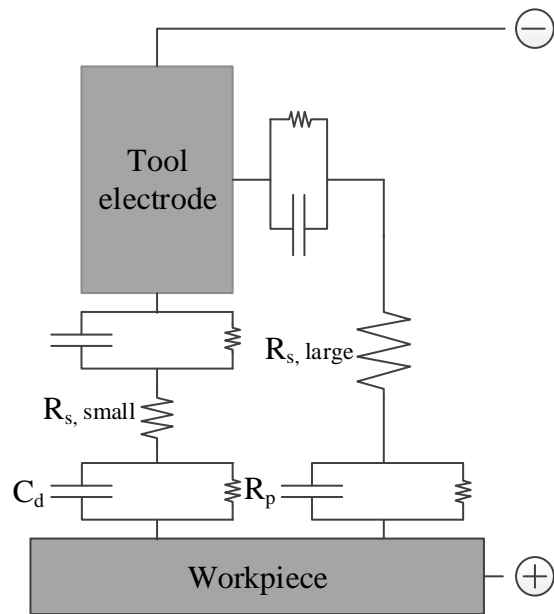


Fig. 2.3 Double layer model[37]

The electrochemical cell with two electrodes of tool and workpiece is illustrated as an equivalent RC circuit in Fig. 2.3 which consists of double layer capacitances C_d , polarization resistances R_p and electrolyte resistance R_s . When ultrashort pulse is applied between two electrodes, it is allowable to take into consideration only transient response. Hence, the polarization resistance can be neglected, so that the equivalent circuit can be simplified into the RC circuit with C_d and R_s . the electrolyte resistance is proportional to the gap distance d . In the region where the distance between electrodes is small, the resistance of electrolyte per unit area, R_s is:

$$R_{s,small} = \rho d_{small} \quad (2.13)$$

where ρ is the specific electrolyte resistance. Where the distance is large, R_s is:

$$R_{s,large} = \rho d_{large} \quad (2.14)$$

The charging time constant τ of the double layer in each region can be expressed as:

$$\tau_{small} = \frac{1}{2} R_{s,small} C_d = \frac{1}{2} \rho C_d d_{small} \quad (2.15)$$

$$\tau_{large} = \frac{1}{2} R_{s,large} C_d = \frac{1}{2} \rho C_d d_{large} \quad (2.16)$$

From these equations, the charging time for the double layer is proportional to the inter-electrode gap. In the small gap d_{small} , the charging time is shorter than in the large gap d_{large} . When pulses with the on-time T ($\tau_{small} \leq T \leq \tau_{large}$) are applied between electrodes, the double layer only in the small gap is charged over the effective potential Φ_{eff} , which is sufficient over-potential for reaction. The double layer potential where the inter-electrode gap is large does not reach the effective potential due to its long charging time, as shown in Fig.2.4 and Fig. 2.5. Since the chemical reaction rate is exponentially proportional to the potential of the double layer, the reaction can be restricted to the region very close to the electrode. This ECM model is feasible at each frequency range of applied electric source.

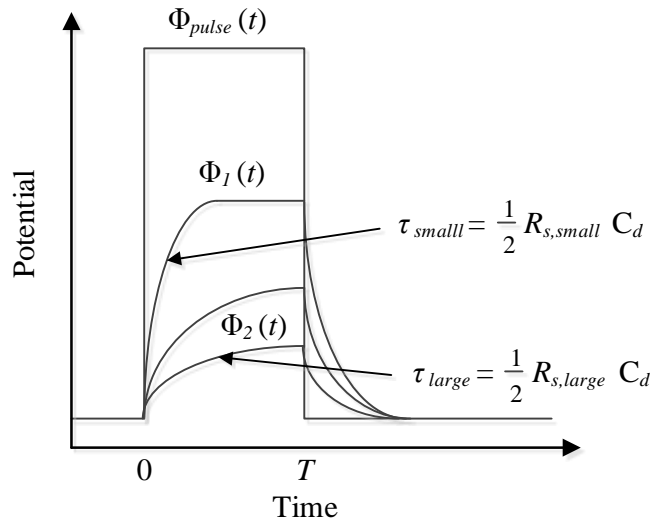


Fig. 2.4 Difference of charging potentials [37]

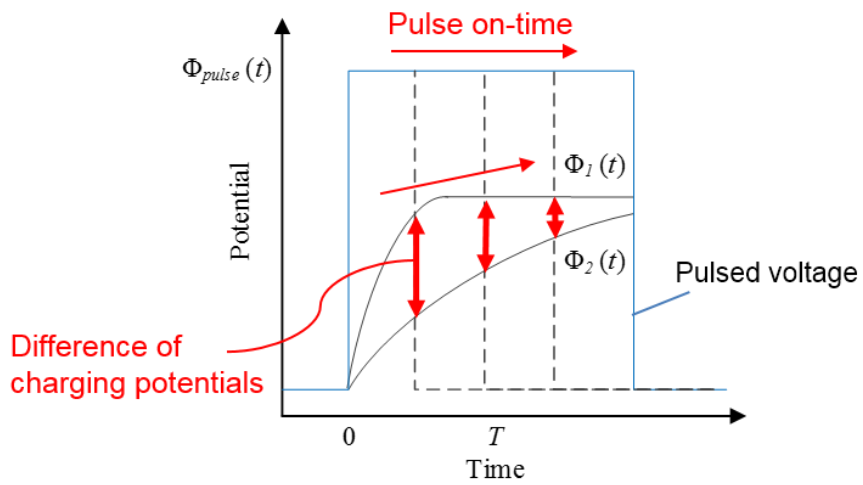


Fig. 2. 5 Difference of charging potentials

2.2 Experimental system

As shown in Fig.2.6, the experimental system consists of the wire electrical discharge machining (WEDM) system and local anodizing system. Two systems were attached to the same three-axis stage with a resolution of 0.1 μm to avoid tool runout. The local anodization system was made up of an electrochemical bath, pulse generator, amplifier, power supply, and tilting stage. A micro cylindrical tungsten carbide (WC) shaft was used as the tool electrode (cathode) and installed on the spindle motor. Since this material is possible to make a straight electrode with a high aspect ratio at the micro scale [38]. The WC shaft with 300 μm in diameter was fabricated by WEDM to obtain a micro electrode with a final diameter (20, 40, 100 μm) and insulated with enamel except for the bottom surface to concentrate the current. Pulses between an electrode and a workpiece were measured by an oscilloscope. As a workpiece, highly pure (99.999 %, Nilaco Co.) aluminum was used and cleaned in $\text{C}_2\text{H}_5\text{OH}$ solution and anodized in $\text{H}_2\text{SO}_4 + \text{C}_2\text{H}_2\text{O}_4$ solution at room temperature(293 K), with a micro second pulse voltage. The tool electrode was scanned above the workpiece retaining a certain distance between electrode

tool and workpiece. In this experiment, X-Y stage and Z stage were used for the three dimensional positioning.

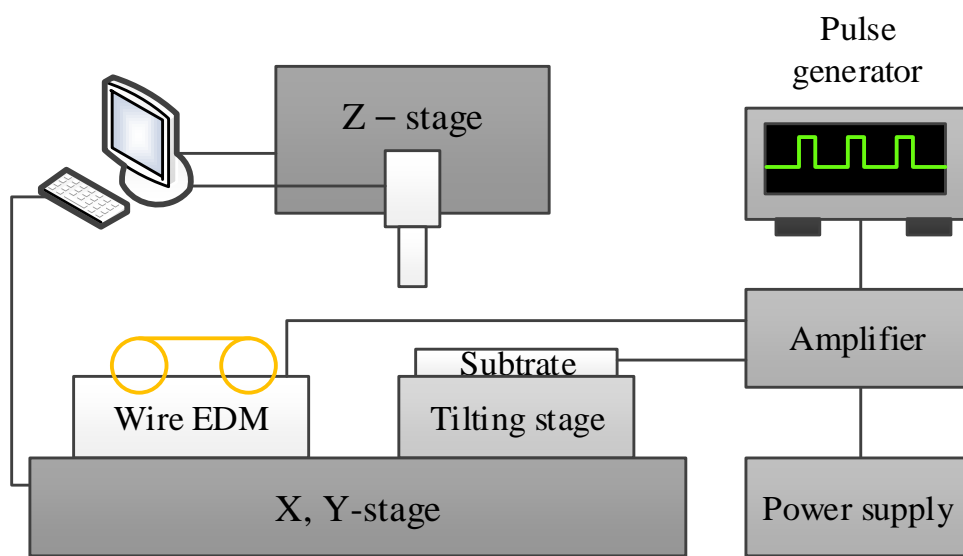


Fig. 2.6 Schematic diagram of experimental system

2.2.1 Positioning system

Since the anodization process is carried on with a very small gap, precise movement and certain inter-electrode gap are important. Hence, the electrode feed should be controlled with micro-meters accuracy. In this research, the X-Y stage is 315082AT stage of Parker Automation. The X-Y stage on which an anodization and WEDM bath were mounted was used to move a workpiece horizontally. The Z stage (4042200XR stage, Parker Automation) control the gap between micro tool and workpiece vertically. Both stages controlled by stepping motors (ZETA57-83, Parker Automation). Linear encoders were attached to control the position with resolution of 0.1 μm /count. All systems were controlled by CEM-Clipper (Delta Tau Data Systems, Inc.) and monitored by PC. The specifications of the stages are shown in table 2.1.

	X-Y stage	Z stage
Model	325082AT Parker Automation	404200XR Parker Automation
Motor	ZETA 57-83 stepping motor	ZETA 57-83 stepping motor
Travel	200 mm, respectively	200 mm
Positional repeatability	1.3 μ m	1.3 μ m
Resolution	0.1 μ m /count	0.1 μ m /count
Limit/home switch	Optical sensor type	Optical sensor type

Table 2.1 Specification of positioning system

2.2.2 Pulse generator

A pulse generator played a role to provide a potential difference between workpiece and tool electrodes. To apply several microsecond pulses, 8551 (Tabor Electronics), of which rising time is minimum 8ns, was used. Generally in the high frequency circuit, input/output impedance are set to be 50 ohms to reduce transmission loss and signal shape distortion. The output impedance of this pulse generator is 50 ohms as well. However the impedance of the electrochemical cell is hard to define, because the electrolyte resistance and the double layer capacitance are varied according to the cell configurations. To minimize the effect of impedance mismatch, a unity gain voltage follower circuit without resistors was connected.

Model	8551, Tabor Electronics
Amplitude	-8 ~ 8V
Pulse width	10 ns ~ 999 ms
Pulse repetition frequency	~ 50 MHz
Rise and fall time	$T_r \leq 6\text{ns}$, $T_f \leq 6\text{ ns}$
DC offset	-8 ~ 8 V
Output impedance	50 Ω

Table 2.2 Specifications of the pulse generator

2.2.3 Fabrication of tool electrode

To fabricate micro aluminum oxide pattern, tool electrodes should be precisely machined. As a technique to fabricate micro electrodes, wire EDM (WEDM) was employed, which is used to machine electrically conductive materials such as steel, graphite, silicon and magnetic materials in the simple way [39]. WEDM is applied for the machining of micro electrode which has uniform diameter as shown in Fig. 2.7. A wire is fed along the wire guide, so the tool wear is negligible [40]. Using this method, a micro electrode of tens of micro meter in diameter can be fabricated within 3 μm errors. The WC shaft with 300 μm in diameter was fabricated by WEDG to obtain a micro electrode with a final diameter (20, 40, 60 μm) and insulated with enamel except for the bottom surface to concentrate the current as shown in Fig. 2.8 (a). The fabricated tool electrode is shown in Fig. 2.8 (b).

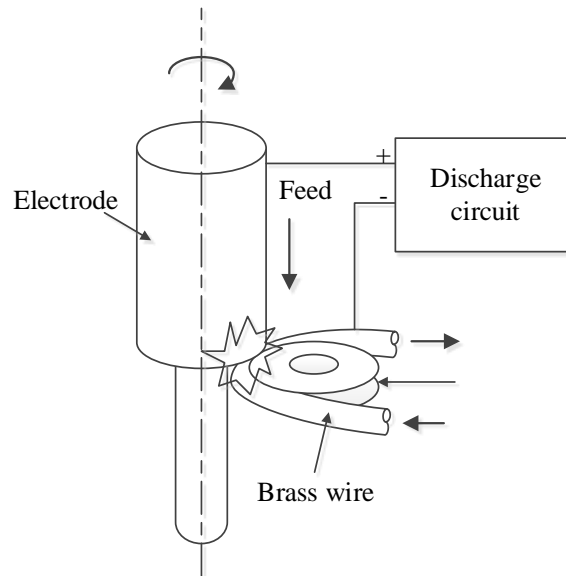
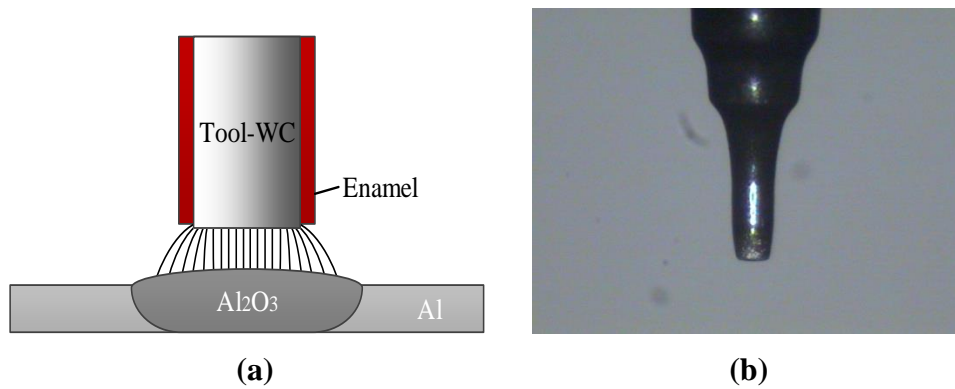


Fig. 2.7 Schematic diagram of WEDM for fabrication of micro electrode



**Fig. 2.8 Fabricated tool electrodes: (a) schematic of tool electrode,
(b) fabricated ϕ 40 μm tool electrode**

Chapter 3

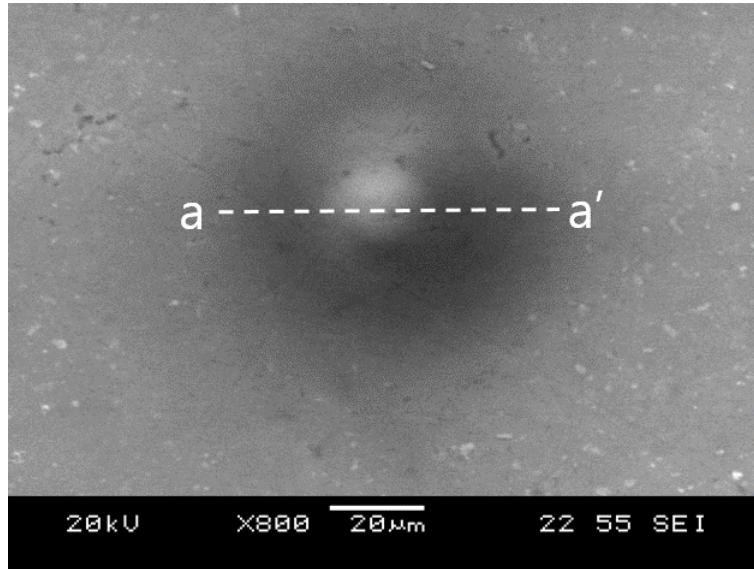
Characteristics in local anodization

3.1 Oxide growth

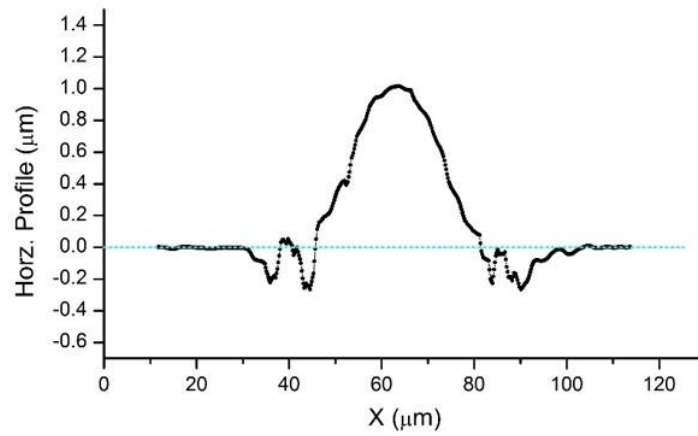
The local anodization was carried out at one point on the aluminum surface using 20 μm diameter tool electrode and confirmed creation of oxide. Fabricated oxide was analyzed by the field-emission SEM including energy dispersive spectroscopy (AURIGA FE-SEM, Carl Zeiss). To minimize local shortage of ions and supply fresh electrolyte, tool electrode was rotated at 240 rpm. The tool electrode moved down from a height of standby position to anodizing position for 2 min. Detail experimental conditions are determined by the parameters as shown in Table. 3.1. Fig. 3.1 shows the SEM and 2D surface profile (a-a') images of dome-shaped aluminum oxide. The anodized area is about 40 μm in diameter and 1 μm higher than the height of the substrate surface. It means a local area of the aluminum is sufficiently anodized.

Parameters	Condition
Substrate material	500 μm thickness 99.999 % aluminum
Electrolyte	0.5 M H_2SO_4
Tool diameter	20 μm , 40 μm
Applied voltage	18 V
Pulse on time	1 μs
Pulse period	10 μs
Anodizing time	120 s
Inter-electrode gap	10 μm

Table 3.1 Conditions of local anodization



(a)



(b)

Fig. 3.1 Aluminum oxide formed by local anodization: (a) SEM image of aluminum oxide, top view, (b) 2D surface profile of section a-a'

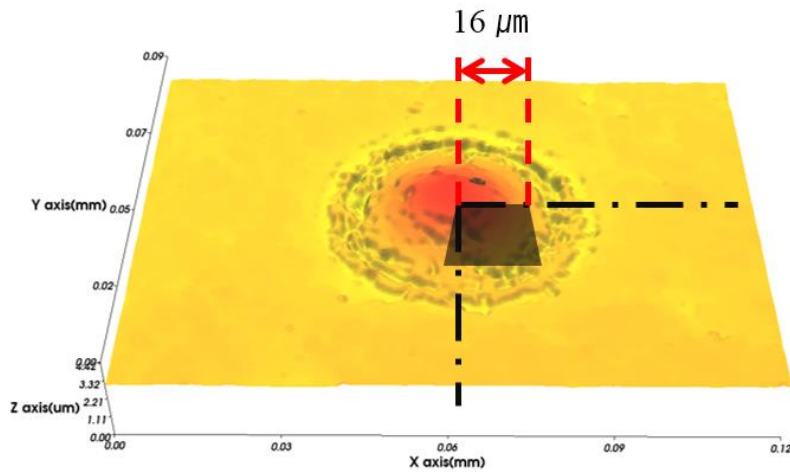


Fig. 3.2 3D surface profile of the localized aluminum oxide

To observe the inside, the right half cross section of the symmetrical oxide was etched by Focused Ion Beam (FIB, AURIGA, Carl Zeiss) after sputtering the platinum to protect the surface from FIB (Fig. 3.2). As shown in Fig. 3.3, aluminum oxide was formed with about 5.2 μm depth and interfacial line between oxide (dark area) and aluminum (lighter area) layer is clearly distinguished. The curve of the interfacial line indicate an electric field level caused by electrode and workpiece.

Fig. 3.4 shows the energy dispersive spectroscopy (EDS) and profile images of the oxide in Fig. 3.3. EDS spectra profile analysis provides the elemental

composition maps of materials. EDS spectra of aluminum (green) and aluminum oxide (red) where the oxygen peak appears (Fig. 3.4(b)). As a result, it is confirmed that the number of micro-depth localized aluminum oxide was fabricated at specific location on aluminum surface using a micro electrode tool.

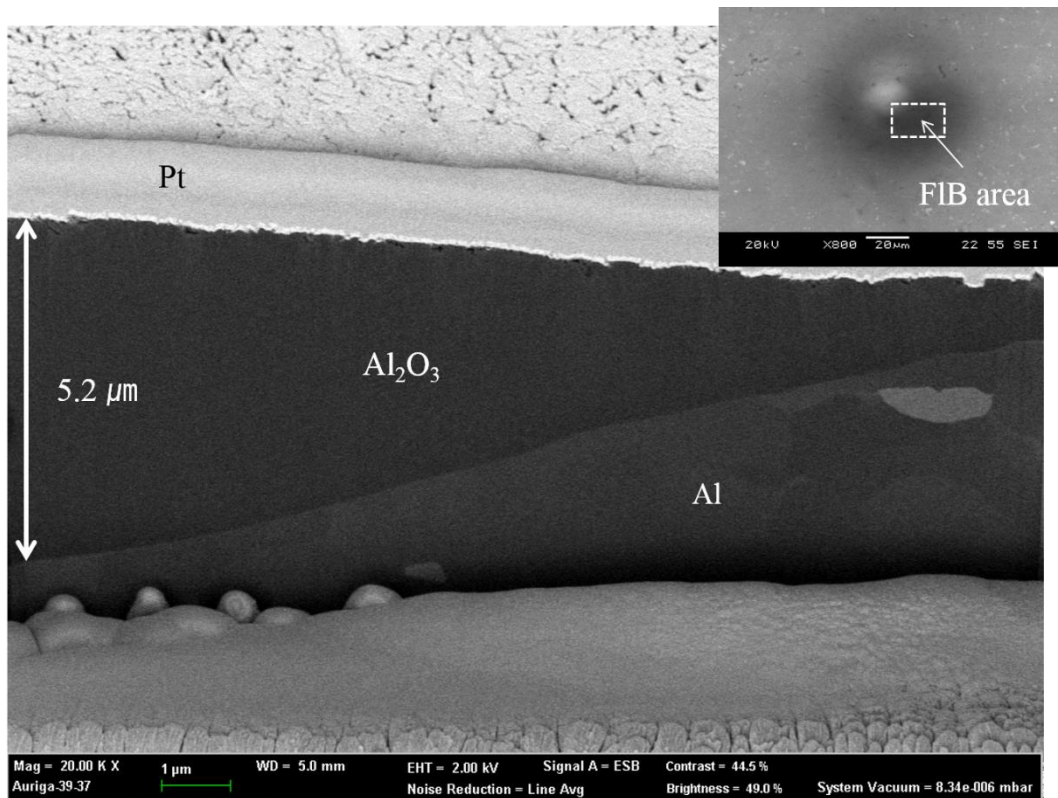
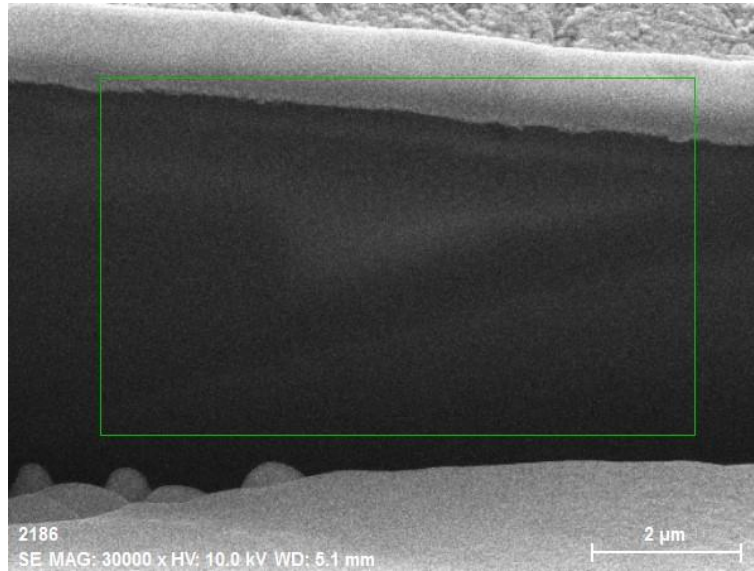
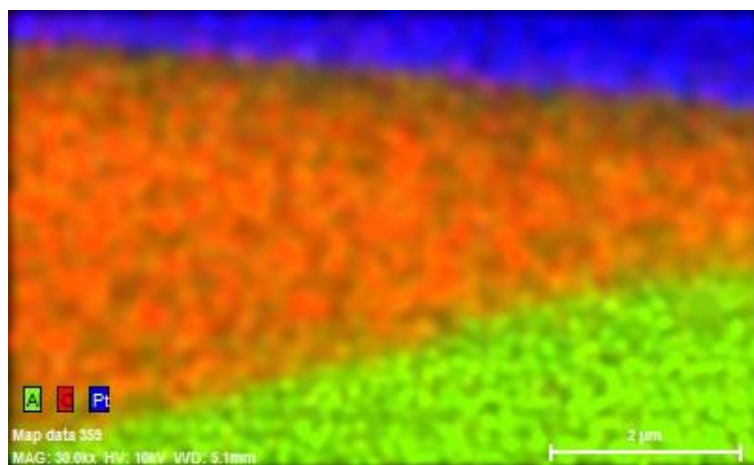


Fig. 3.3 SEM image of the cross section of localized aluminum oxide formed by local anodization



(a)



(b)

Fig. 3.4 Analysis of the cross section of aluminum oxide: (a) Target space of the EDS analysis (b) EDS map data of the surface

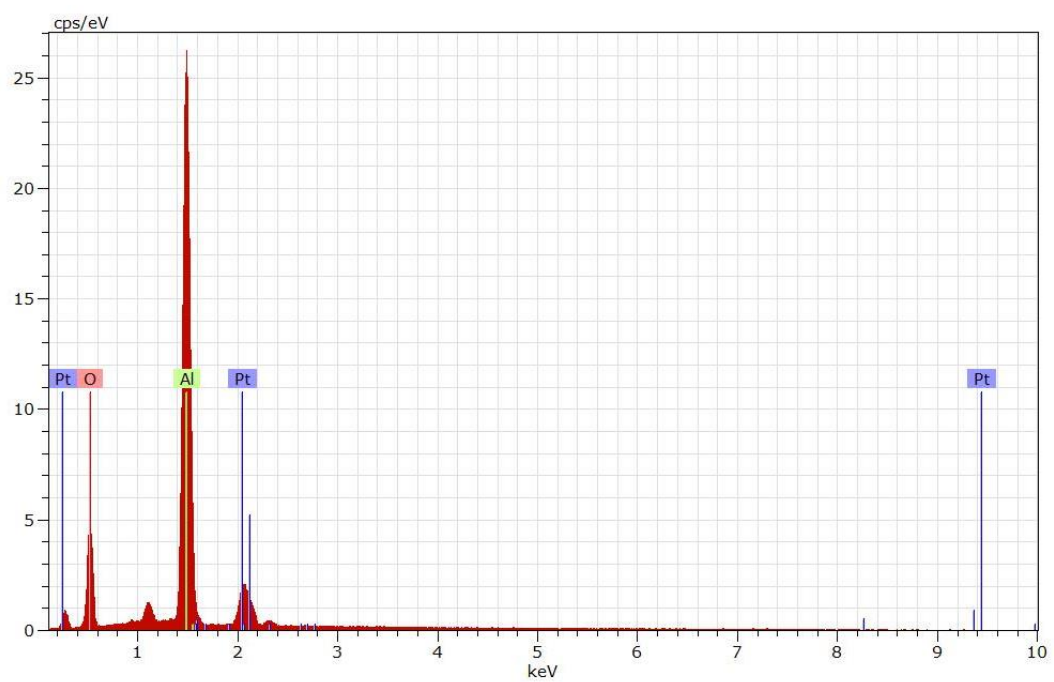


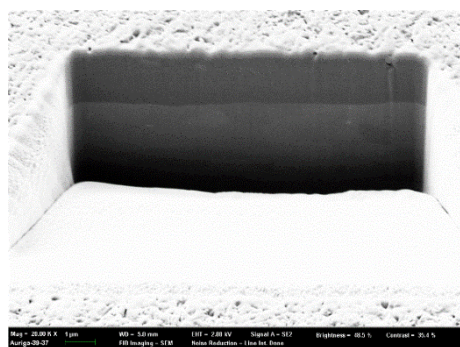
Fig. 3.5 EDS profile of the cross section of aluminum oxide

Formation of the oxide layer

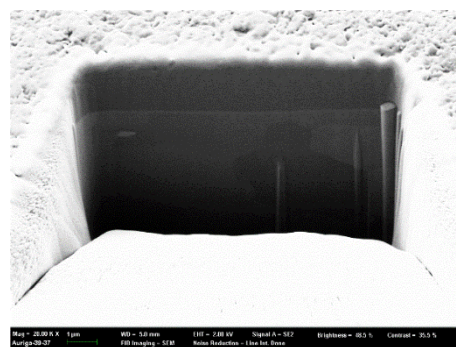
As discussed in chapter 2.1.2, the two main reactions of the formation of the oxide layer are formation of aluminum oxide, and the chemical/electrical dissolution of the oxide layer. Fig. 3.6 and Fig. 3.7 were obtained during the first 120 seconds of the anodization which shows that oxide growth and main reactions according to time. The images in Fig. 3.6 are the cross sections located at center of the oxide and etched by FIB (AURIGA, Carl Zeiss). For better observation of the oxide growth, larger 40 μm diameter tool was used.

Period 0 ~ 30 s in Fig. 3.6 (a) shows that the formation of the first microns of oxide and chemical/electrical dissolution and formation are occurred. Accordingly, height of the oxide become lower than substrate surface. Then the current starts to decrease because of the formation of a thin barrier layer. This oxide layer has a higher resistance than the metallic aluminum. During the period 30~60 s, small imperfections are formed by the concentration of the current in areas with thinner oxide due to higher field assistant dissolution [35]. As shown in Fig. 3.7 (b), overall thickness of the oxide is maintained with about 1.8 μm during 30 ~ 60 s. The imperfections stated that these areas are the places where the initial formation of pores starts. Then, while the oxide thickness is reduced, the height of overall porous

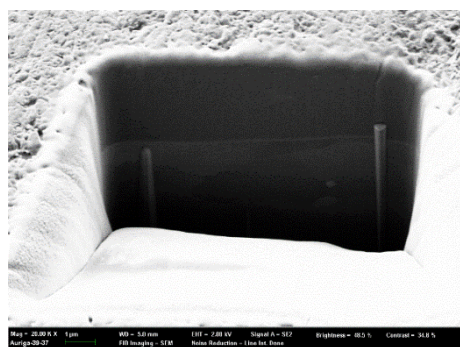
oxide is increased and the current will start to flow to repair the damage, 60~90 s [35]. Then, during the 90 ~ 120 s, A thick oxide layer raise the temperature of electrolyte around the barrier layer and it will lead to an increase in the rate of chemical dissolution. The depth of the barrier layer has reached a level where the field strength has increased enough and suddenly the current increases steeply [35]. It makes local crack on the barrier and electrical/chemical dissolutions are occurred again. As a result, depth of the oxide is deepen continuously.



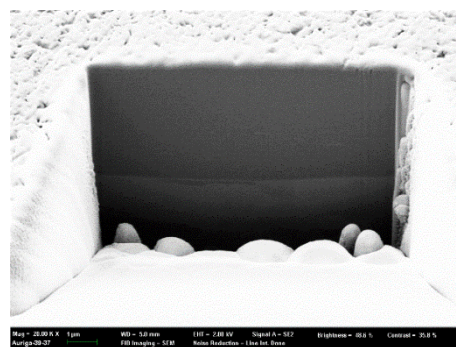
(a) 30 s



(b) 60 s

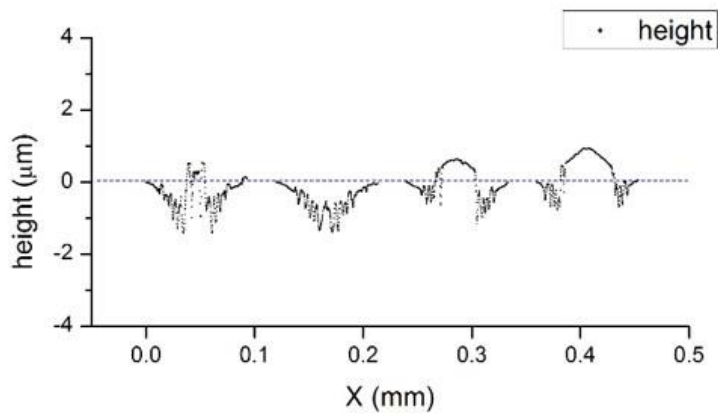


(c) 90 s

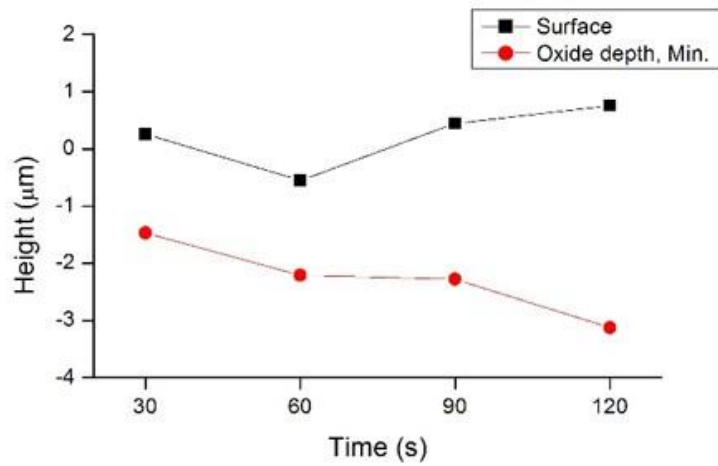


(d) 120 s

Fig. 3.6 FE-SEM images of the cross section of center of the oxide



(a) 2D surface profile of the oxide: 30 s, 60 s, 90 s, 120 s.



(b) Height of the oxide surface and depth

Fig. 3.7 The height of the oxide according to time

Structure of the oxide layer

Observing the cross section of the fabricated oxide layer, the porous structure is not visible as shown in Fig. 8. That is dense oxide structure as seen in the hard anodizing [7]. Hard anodizing or hard coat are known as anodizing Type III, which enables aluminum surface to have thick oxide layer. Anodizing thickness increases wear resistance, corrosion resistance, ability to retain lubricants, and thermal/electrical insulation. During the hard anodizing, a uniform aluminum oxide layer is formed on the surface that penetrates into the material in sulfuric acid alone or with additives. The acid and the applied electric field condition in local anodization is similar to hard anodizing condition, thus dense aluminum oxide can formed. When compared to previous studies, as shown in Fig. 3.9 (pore oxide) and Fig. 3.10 (dense oxide), it is certain that the oxide layer fabricated by local anodization is that of hard anodizing.

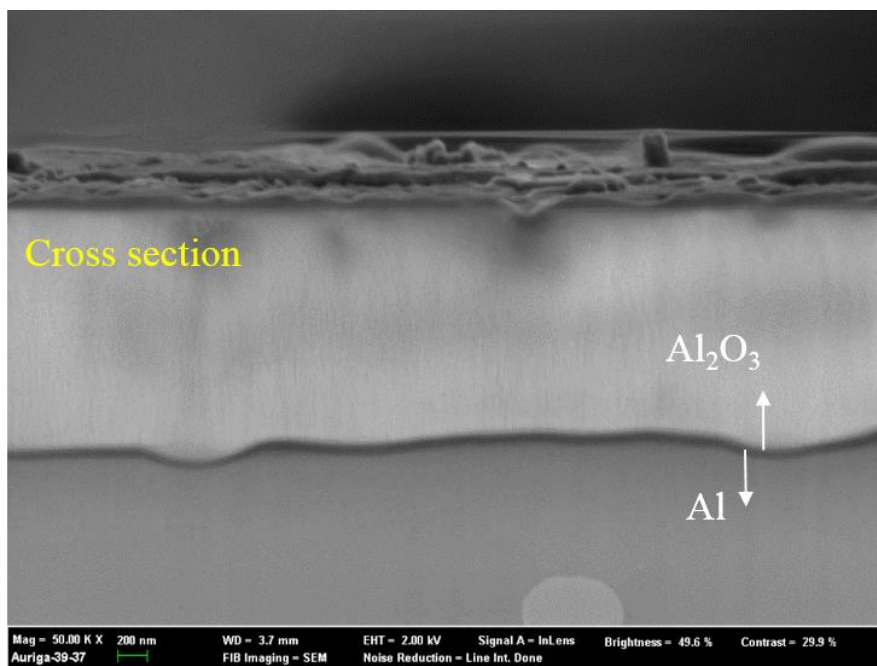


Fig. 3. 8 FE-SEM images of a cross section and surface of localized aluminum oxide (etched by FIB)

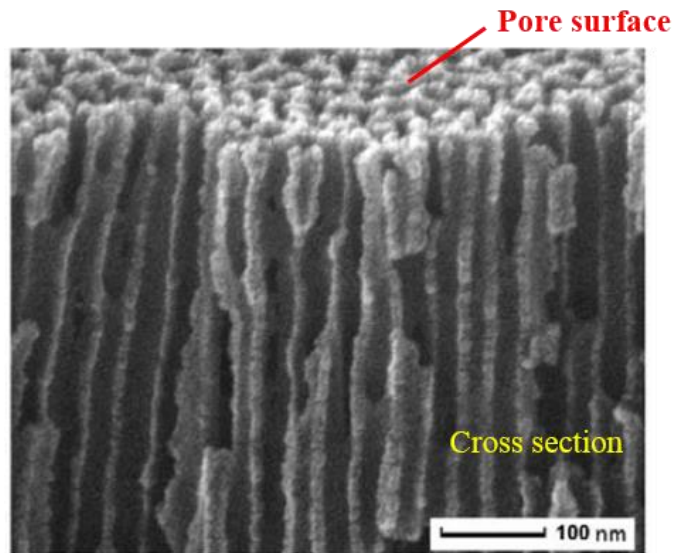


Fig. 3. 9 FE-SEM image of a cross section of a porous oxide layer (near the surface) [41]

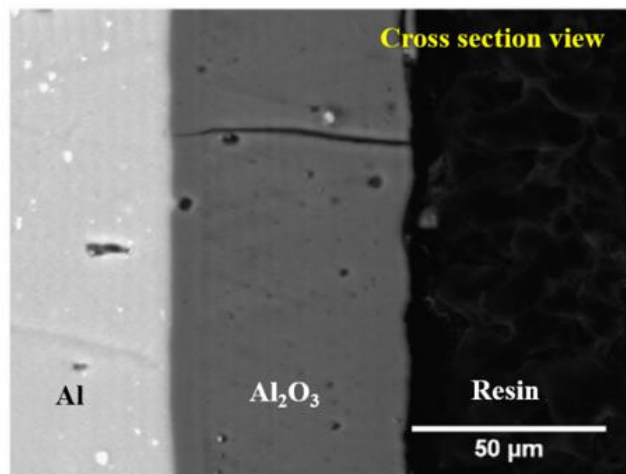


Fig. 3. 10 BSE micrographs of cross section and dense oxide layer [42]

Hardness of the oxide layer

Fabricated oxide layer can act as not only an electric insulator but also a supporting of the electric circuit structure. Thus the mechanical characteristic of aluminum oxide was measured with indentation hardness test. Indentation is the most commonly applied means of testing the mechanical properties of materials. The nano-indentation technique was developed to measure the hardness of small volumes of material. The maximum loading depth cannot be more than 10 % of the sample thickness, tested depth was 150 nm, because the thickness of oxide layer are 2~10 μm . Berkovich diamond tip was used for indenter and sample the data from the 6 points of the oxide surface. Detail experimental conditions are determined as shown in table 3. 2. The load depth curves results is shown in Fig. 3. 11. From extracting 6 sample data, 7.295 GPa and 109.96 GPa were gained for mean indentation hardness (HIT) and mean indentation modulus. Generally, oxide in hard anodizing condition have 3 to 10 GPa hardness and 90 to 200 GPa modulus. As a results, the oxide layer fabricated by local anodization can support circuit structure and provides higher stiffness.

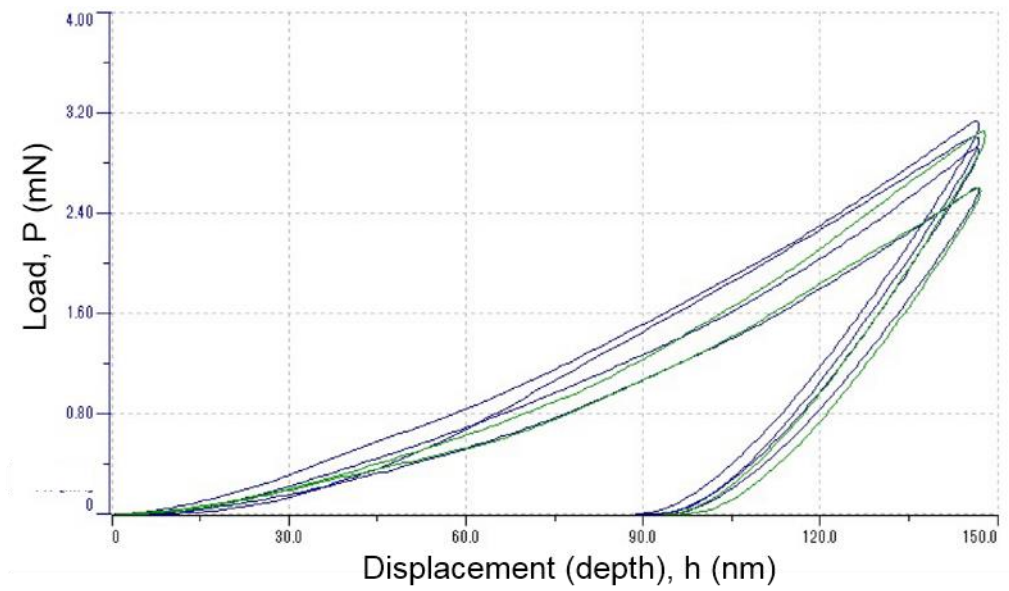


Fig. 3. 11 Load-depth curves of localized oxide by nano indentation test

Test condition and results	
Indenter	Berkovich diamond tip
Loading	Linear loading
Max. depth	150 nm
Applied voltage	1 $\mu\text{m}/\text{min}$
Sampling data	6 point
HIT (Indentation hardness, Mean)	7.295 GPa
EIT (Indentation modulus, Mean)	109.96 GPa

Table 3. 2 Conditions and results of the nano-indentation

3.2 Gap between tool electrode and workpiece

Theoretically, in ECM, shorter gap between tool electrode and workpiece has advantage of localizing reaction. However, electrolyte should be filled between electrodes and generated bubble during chemical reaction prohibit next chemical reaction. Therefore, the gap cannot be set extremely short. Moreover, in local anodization, too high electric field density may cause trouble as the burning phenomenon. Therefore, to investigate the oxide characteristics according to gap, anodization tests were performed by varying inter-electrode gap under the same conditions of chapter 3.1.

The test gap is in the range from $5\mu\text{m}$ to $20\mu\text{m}$. In more than $15\mu\text{m}$, thickness of the oxide was sharply decreased and localized oxide boundary were blurred as shown in Fig. 3.12 오류! 참조 원본을 찾을 수 없습니다.. Moreover, unwished thin oxide layers were formed on the surrounding surface. According to double layer theory, as inter-electrode gap increase, maximum charging voltage is decreased. (Fig. 3.13)

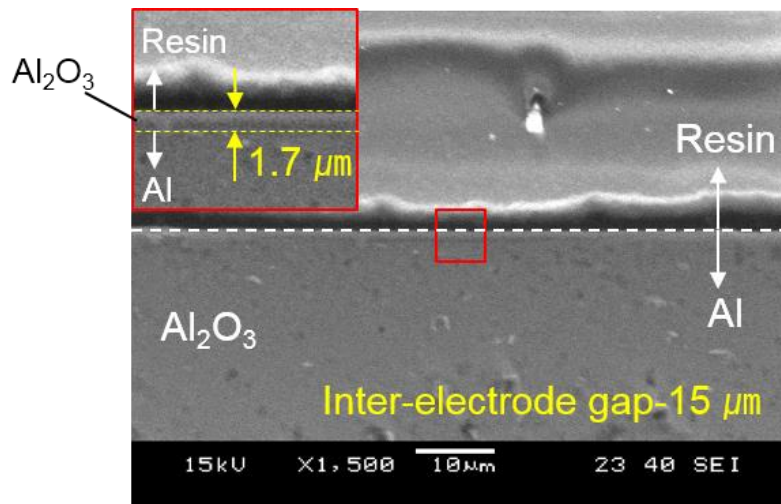


Fig. 3. 12 SEM image of oxide 15µm inter-electrode gap at 20 V

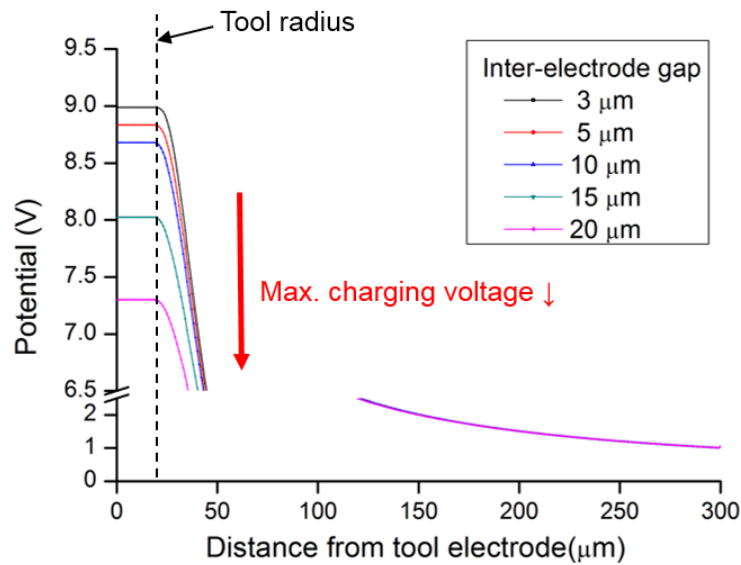
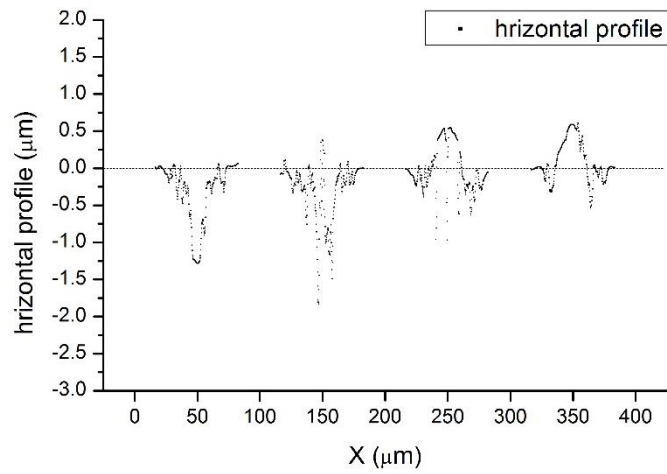


Fig. 3. 13 Simulation results of Φ_c according to distance

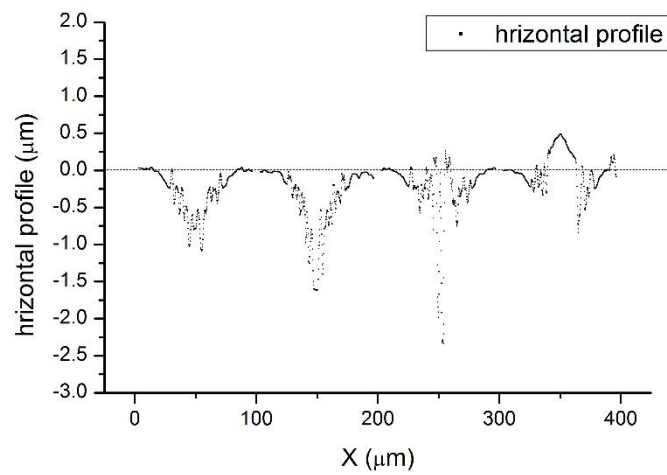
Some prominent results were in test at 5μm and 10μm gap. Fig 3. 14 shows comparative experimental results of surface profile according to anodization time. In terms of localization, in a sense of ECM, anodized area (at 5μm gap) was about 15 μm smaller in diameter than that of 10 μm. It is presumed that shorter inter-electrode gap causes narrower electric field projection.

On the other hand, at 5 μm condition, electrical/chemical dissolution step was ended earlier and further the depth of dissolved aluminum was also smaller than that of 10μm. In comparison at the beginning of the 30 s, dissolution of aluminum

is larger in 5 μm condition, but in after 30 s, pore layer began to be formed. As discussed in chapter 3.1, when the pore structure is begin to formed, formation speed of the oxide to depth direction slows down. To make sure the exact reason of this phenomenon in higher electric density, further studies will be required. However, in this dissertation, the results will be applied to fabricate the micro oxide line.



(a) Gap : 5 μm, 30 s, 60 s, 90 s, 120 s



(b) Gap : 10 μm, 30 s, 60 s, 90 s, 120 s

Fig. 3. 14 Localized oxide surface according to time (a) 5 μm gap, (b) 10 μm gap

3.3 Ratio and concentration of electrolyte

Generally, in anodizing process, conditions such as electrolyte concentration, acidity, solution temperature must be controlled to allow the formation of consistent oxide layer. In conventional anodizing, highly concentrated sulfuric or oxalic or chromic electrolyte is used for fast process of aluminum [5]. In local anodization, however, electrolyte and concentration should be chosen carefully, considering the oxide width, oxide depth and undesired corrosion of surrounding surface.

In many studies of the fabrication of nanopore structure on aluminum, the sulfuric/oxalic electrolyte has been used for first anodizing process to larger the pore size, barrier layer thickness and cell size [17]. However, in this process, highly corrosiveness of sulfuric acid is inappropriate in terms of localizing and oxalic acid act as a buffer for the drastic anodization [17].

In highly diluted sulfuric acid electrolyte, naturally, the anodized area is localized as shown in Fig. 3.15.

Table 3.3 EDS analysis of area 1, 2 in Fi. 3.8 (b) Table 3.3 shows the EDS analysis of area 1, 2 (violet square), area 2 is anodized oxide the tool electrode passed above.

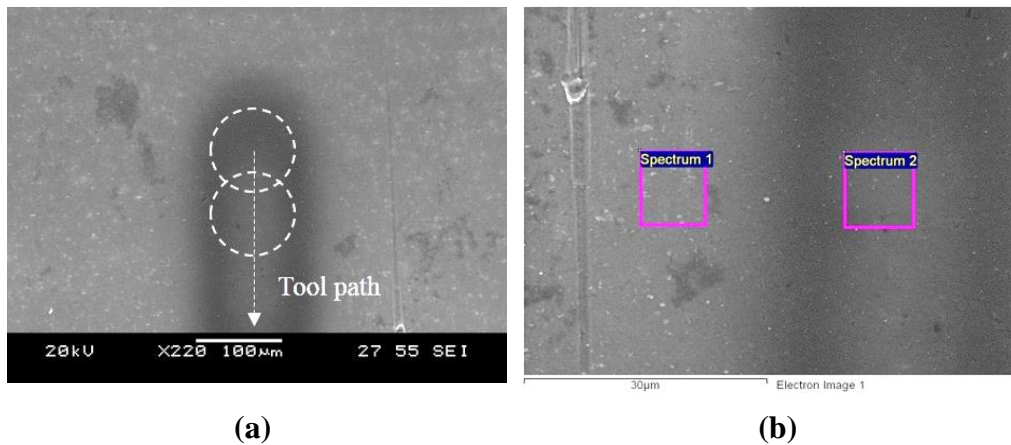
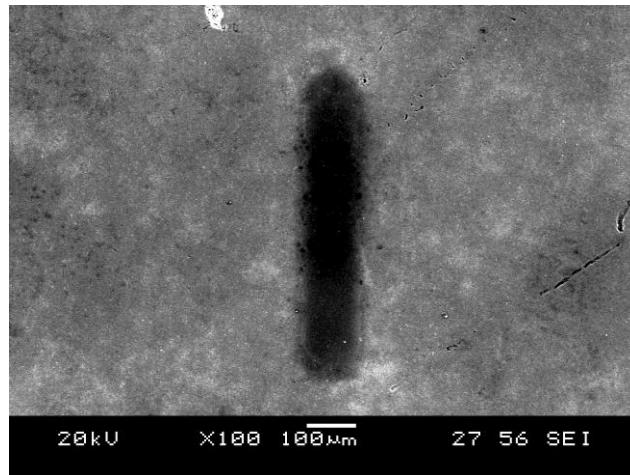


Fig. 3.15 SEM image of the local anodization in 0.1 M H₂SO₄ electrolyte

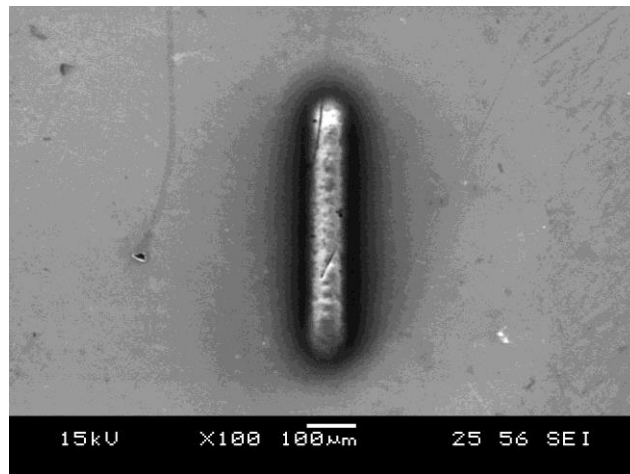
Spectrum 1			Spectrum 2		
Element	Weight %	Atomic %	Element	Weight %	Atomic %
O	3.91	6.41	O	49.02	61.85
Al	96.09	93.59	Al	50.98	38.15

Table 3.3 EDS analysis of area 1, 2 in Fi. 3.8 (b)

However, in more than 0.5 M concentration electrolyte, anodized area was wider even in low applied voltage. As shown in Fig. 3.16, Oxide layer is not formed at high voltage in 0.1 M H₂SO₄ acid electrolyte. On the contrary, in 1 M H₂SO₄ acid electrolyte, aluminum oxide formed in wide area even in low voltage. In this reason depth and width of the anodized oxide were investigated in different ratios of 0.5 M sulfuric and 0.5 M oxalic acid mixtures at various applied voltage condition. Experimental range of applied voltage and anodization time are chosen by reason of avoiding the burning and powdering phenomena [43]. To be precise, the burning is due to a high current density and it lead destruction of the local barrier oxide layer [19]. Powering effect is due to a combination of long anodization time and high concentration of the electrolyte [43]. The acidic electrolyte will dissolve the aluminum oxide. Since the chemical dissolution is independent of the electrical field the attack on the oxide will happen everywhere on the surface. Consequently, these bring the weakening of the barrier and pore oxide structures. However, major causes of these phenomena are compensate each other (the current density, concentration of the electrolyte). Therefore, investigation of concentration of electrolytes and voltage was carried out.



(a)



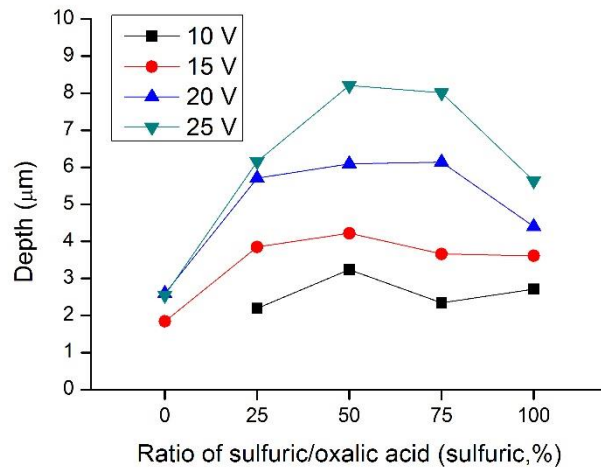
(b)

Fig. 3.16 Anodized aluminum oxide line in different concentration of electrolyte (a) 0.1 M H₂SO₄, 20 V (b) 1 M H₂SO₄, 10 V

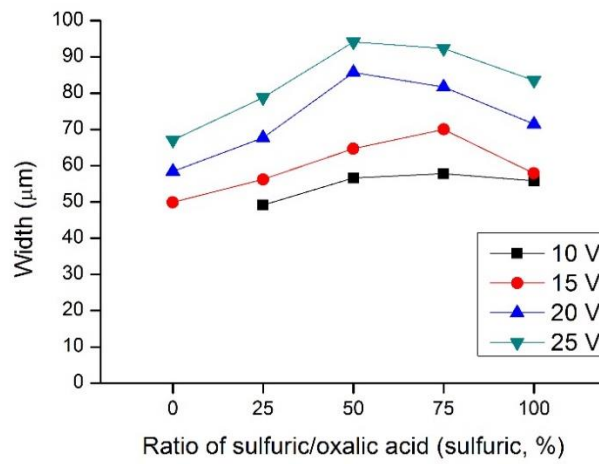
Fig. 3.17 shows the measured depth and width graph of the anodized oxide from specimen surface in different ratios of solution. To see the cross section of the oxide and measure the thickness and depth, it was polished by chemical mechanical polishing. Detailed anodizing conditions are described in Table 3.4.

Parameters	Condition	Parameters	Condition
Workpiece	t 500 μ m, 99.999 % Aluminum	Electrolyte	0.5 M H ₂ SO ₄ + 0.5 M C ₂ H ₂ O ₄
Tool diameter	40 μ m	Feed rate	0.7 μ m/s
Pulse on time	1 μ s	Pulse period	10 μ s
Applied voltage	10 V ~ 25 V	Inter-electrode gap	10 μ m

Table 3.4 Conditions of local anodization



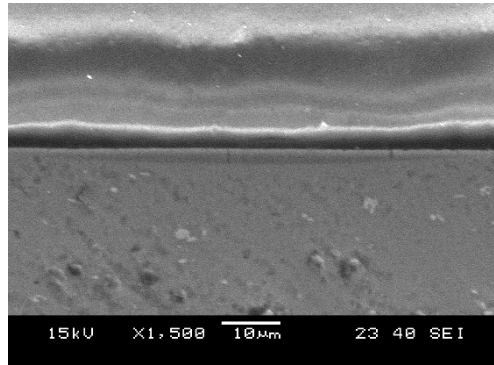
(a)



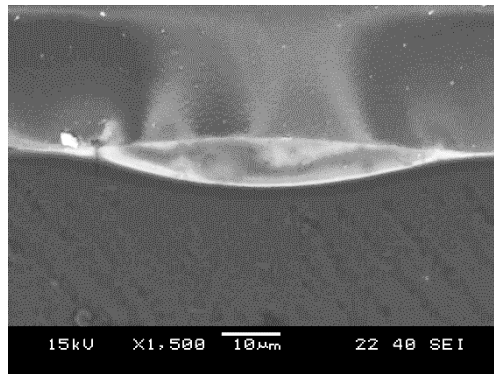
(b)

Fig. 3.17 Depth and width of the anodized oxide in different ratio of $H_2SO_4/C_2H_2O_4$ acid mixtures

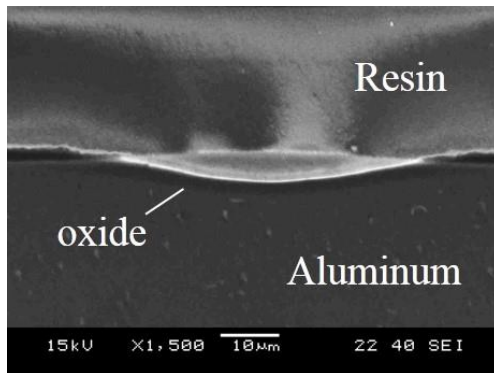
As shown in Fig. 3.17 (a), depths of anodic oxides in mixtures of sulfuric/oxalic acid solutions are deeper in comparison with in sulfuric and oxalic acid. SEM images in Fig. 3.18 presents a large difference of oxide thickness and depth according to ratio of the electrolytes mixtures at 25 V. The exact reasons are unknown, but as discussed, highly corrosiveness of sulfuric acid and buffer capacity of oxalic acid may keep the balance [44]. The changes of depth at 15, 20 V are comparatively slight, while the oxide width difference is noticeable. It shows that the further away from the center of tool electrode bottom, electric field density between the tool electrode and workpiece will decreased. And chemical dissolution take place a dominant anodizing reaction, thus in 20 V (blue line), formation of oxide will be a width direction than depth direction.



(a)



(b)



(c)

Fig. 3. 18 SEM images of cross section of the oxide line at 25 V (a) $C_2H_2O_4$ (b) $C_2H_2O_4 + H_2SO_4 = 1:1$ (c) 0.5 M H_2SO_4

3.4 Pulse conditions

In general anodizing process, pulse anodizing instead of using the same value during the process gives several possibilities for individual process conditions. Many researchers have made suggestions of how these square wave pulses should be designed [43, 45, 46]. They claimed that by pulsing between high and low voltage/current it is possible to increase wear resistance and corrosion resistance. Further pulse anodizing bring a reduction in total anodizing time and the possibility of avoiding burning and powering problems. In their research, applying duration of pulses was varying from 10 – 180 seconds.

On the contrary, for localization, the ultra-short pulse condition is one of the important factors. In micro ECM, the pulse on-time of applied voltage is tens to hundreds of nano seconds [36, 47, 48]. The main reaction of ECM is electrochemical dissolution of material, thus resistance of metal/electrolyte interface does not change significantly. However, in anodization, resistance of thin protective oxide layers prevent the current. This means that higher over-potential will be required so the longer pulse on-time range than that of micro ECM was

investigated. A pulse can be described with pulse amplitude, pulse on-time, pulse off-time voltage and pulse period as shown in Fig. 3.19. Each factor affects the anodization characteristics. It is desirable that the workpiece is anodized fast at pulse on-time voltage, but the anodization is suppressed at pulse off-time voltage. During the anodization, hydrogen gas is created in the interface between aluminum and the barrier layer and can destroy part of the barrier layer oxide. The destroyed parts are the weak places in the barrier layer, which leads to micro cracks. These micro cracks will diminish the resistances of the barrier layer, hence the forming voltage will be less than in anodizing using a DC voltage [46]. Therefore, short pulse is useful not only for localization, but also for anodization. As discussed before, in too short pulse on-time and low pulse amplitude, aluminum will hardly be anodized due to the high resistance of the oxide layer. Thus anodization characteristics in various pulse on-time were investigated. Duty ratio of applied pulse was held constant of 1:10 to apply the same average voltage. Depth and width of the oxide line were measured in different voltages.

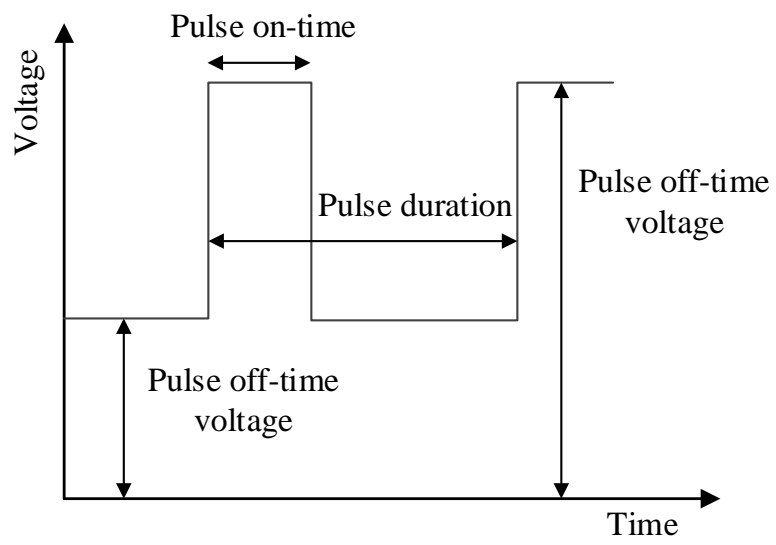
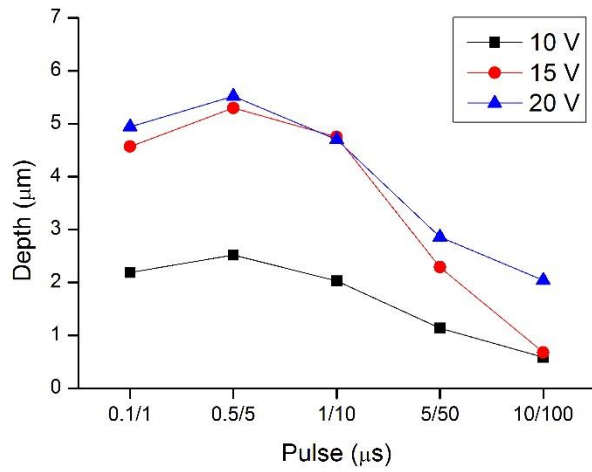
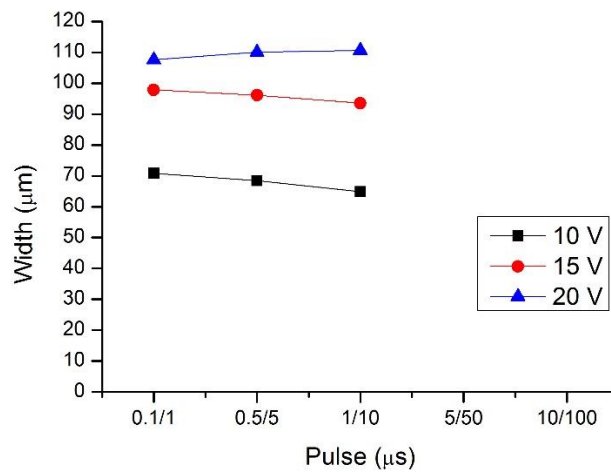


Fig. 3.19 Pulse signal

Fig. 3. 20 (a), as the pulse on-time increase, current cannot be concentrated, thus depth of oxide is decreased. As shown in Fig. 3. 20 (b), width of the anodized oxide is independent of pulse on time. By electrical double layer theory, when the step voltage is applied, as the pulse width decreases, the charging voltage also decreases. According to butler-volmer equation, the electrochemical reaction rate is exponentially proportional to charging voltage as shown in Fig. 21. However, in 0.1 μ s condition is too short for charging, thus the charging potential is lower than that of in 0.5 μ s. Therefore, electrochemical reaction that is anodization is suppressed with short pulse width.

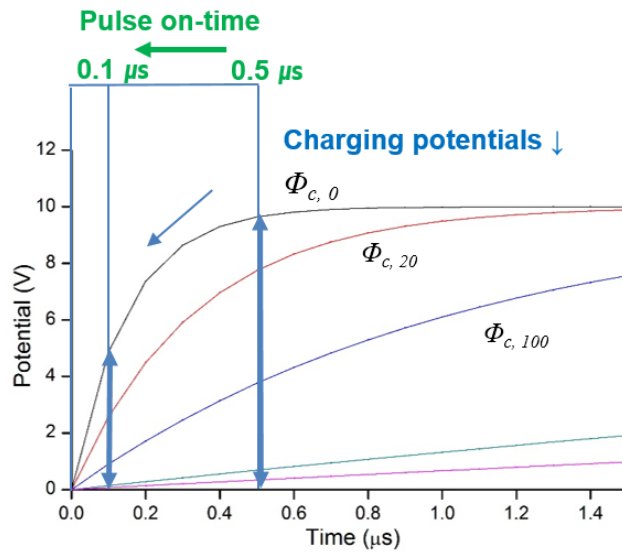


(a)

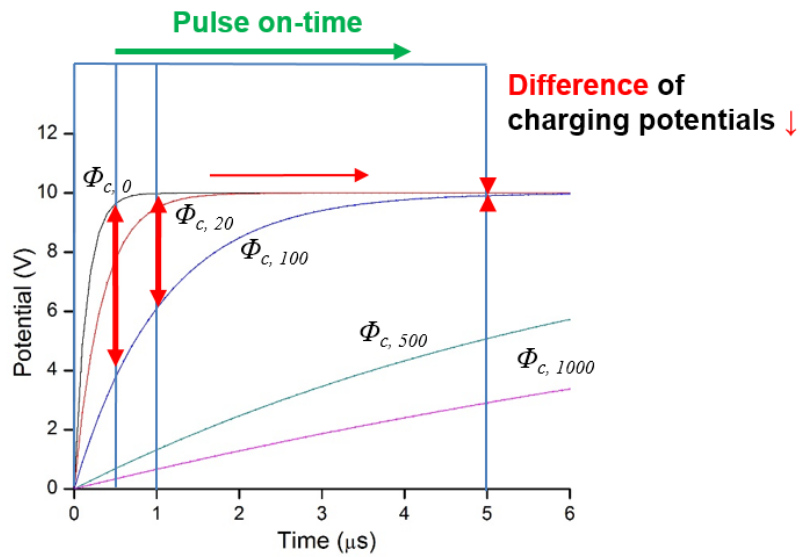


(b)

Fig. 3.20 Depth and width of the anodized oxide in different pulse on-time



(a)



(b)

Fig. 3.21 Charging voltage according to pulse on-time

Chapter 4

Fabrication of aluminum oxide pattern and application

4.1 Fabrication of aluminum oxide pattern

4.1.1 Local anodization conditions

Local anodization is applied to fabricate aluminum electric circuit. As mentioned in the previous chapter, anodizing gap, ratio of the electrolyte mixtures, applied voltage, and pulse on-time should be chosen carefully. In fabrication of oxide pattern, tool electrode moves slowly through line path maintaining the inter-electrode gap. To fabricate the oxide having sufficient thickness, more than 60 seconds anodizing time were required. Therefore, tool feed rate was changed according to tool diameter. As shown in Fig.4.1, the tool electrodes move on the

point –A during $t_1 \sim t_3$, and moving distance is equal to tool diameter. Thus, feed rate can be calculated by

$$\text{Feed rate} = \text{Tool Diameter} / t_{ano} \quad (4.1)$$

where t_{ano} is the required anodization time. Total length of one oxide line pattern in this dissertation is more than 4 mm, to fabricate this pattern using the 40 μm tool electrode, feed rate and total anodization time will be 0.67 $\mu\text{m/s}$ and about 100 minutes. When the proportion of sulfuric acid increases in mixed solution, aluminum surface can be damaged in that long anodization time. Therefore, 25 % sulfuric/oxalic acid mixtures is used for fabrication of oxide pattern. For thick oxide depth, the inter electrode gap was set to 10 μm , and pulses with 20 V, 5 μs duration, and 500 ns period were applied.

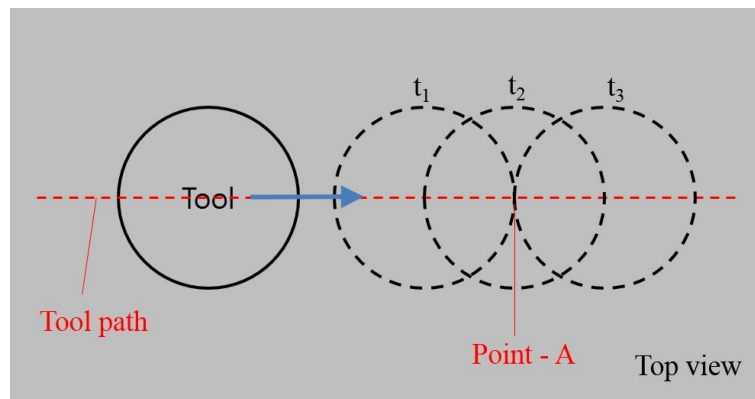


Fig.4.1 Exposure time of the point on the path line

4.1.2 Fabrication of aluminum oxide pattern

Fig. 4.2 shows a micro oxide line pattern which was fabricated by local anodization. The workpiece material is AL1000 (99.999% aluminum) and ϕ 40 μm tool electrode was used. The size of oxide pattern is 1 mm x 1mm, and line width is about 100 μm . The white line in the figure is the anodized oxide.

To apply this technique to micro electric circuit, penetrating oxide line is required and it should disconnect the current. Fabrication of penetrating oxide line is carried out on 10 μm thick aluminum sheet. It was expected that the larger the tool electrode diameter, the deeper the thickness of the oxide, and the thickness of the anodized oxide line for 60 s is about 8 μm as shown in Fig. 3.12 (a), ϕ 60 μm tool electrode was used for the penetrating oxide line. Detailed anodizing conditions are described in Table 4.1. As shown in Fig. 4.3, the bottom width of the oxide line is about 60 μm and top is about 130 μm . Fig. 4.4 shows a penetrating see-through porous oxide line, thus it will act as an insulator of electric circuit.

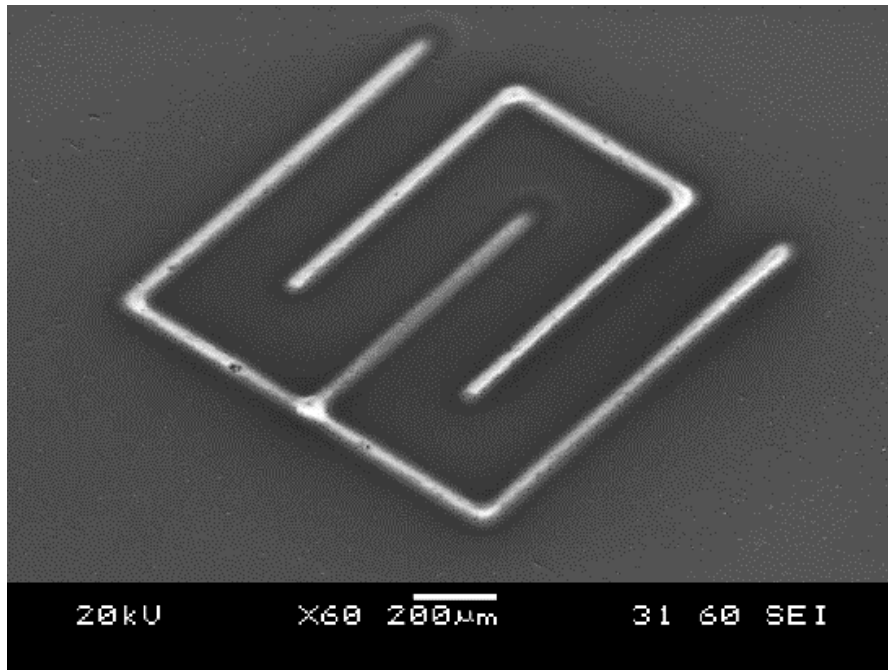
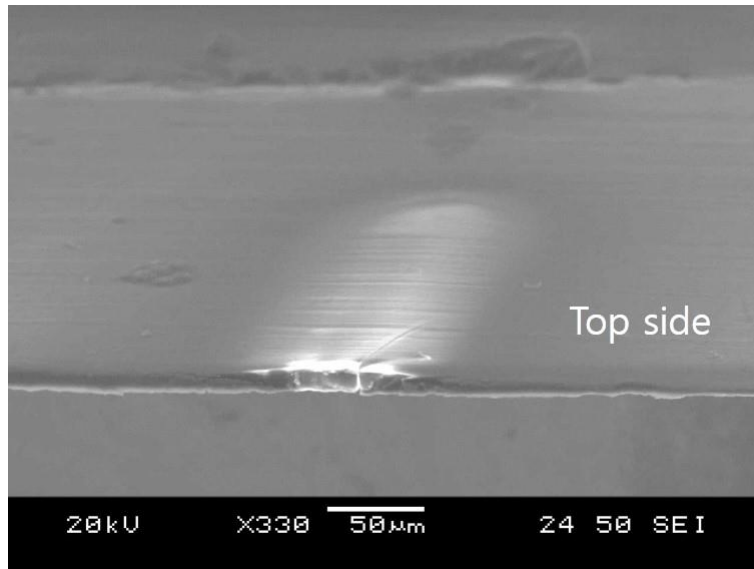


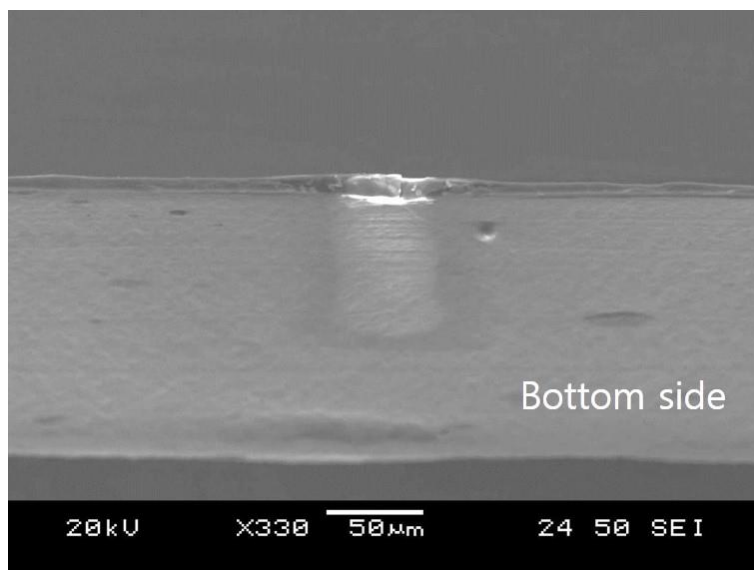
Fig. 4.2 Micro oxide pattern by local anodization (\varnothing 40 μm electrode, 500 μm thick Al sheet, 20 V, 500 ns pulse on-time, 5 μs period)

Parameters	Condition	Parameters	Condition
Workpiece	t 500 μm , 99.999 % Aluminum	Electrolyte	0.5 M H_2SO_4 + 0.5 M H_2SO_4 =1 : 3
Tool diameter	60 μm	Feed rate	1 $\mu\text{m/s}$
Pulse on time	0.5 μs	Pulse period	5 μs
Applied voltage	20 V	Inter-electrode gap	10 μm

Table 4.1 Conditions of local anodization for penetrating oxide line



(a)



(b)

Fig. 4.3 SEM images of the fabricated penetrating oxide line (top, bottom)

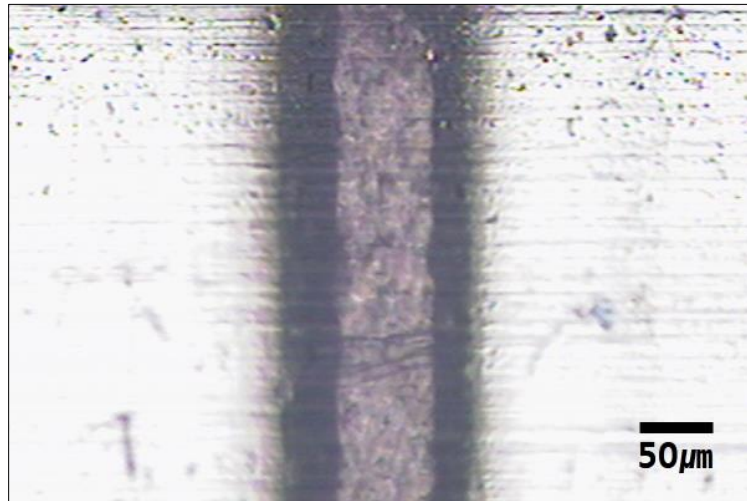
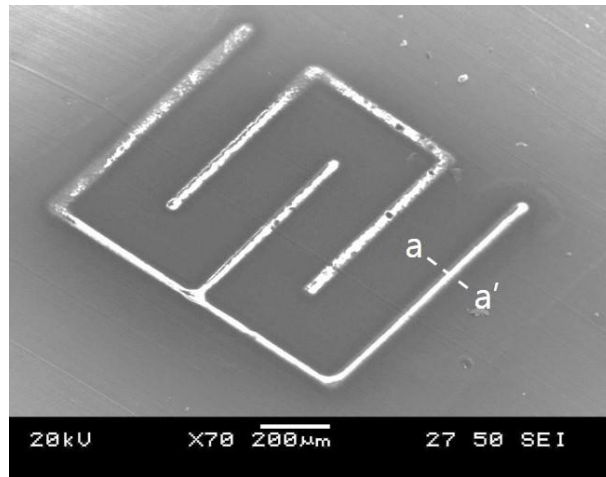
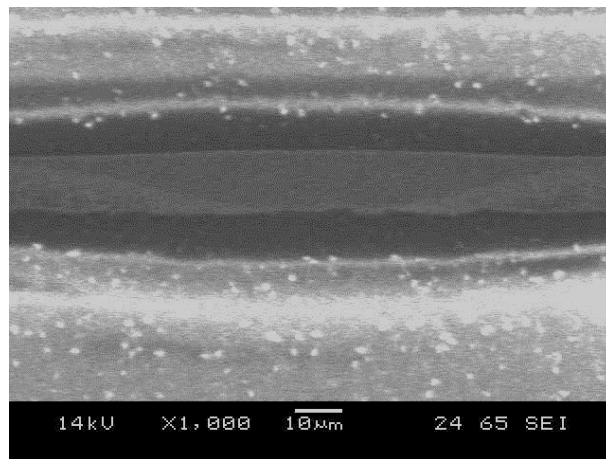


Fig. 4.4 Optical image of penetrating oxide line by local anodization

Using this conditions, penetrating oxide line pattern was fabricated which has same shape in Fig. 4.2. Fig. 4.5 shows that the aluminum surface surround the oxide pattern was not damaged at all, and oxide layer was grown to the bottom. The aluminum path between the oxide pattern can be an electric wire. To measure the performance of the electric circuit using by local anodization, it was applied at RF patch antenna, and discussed in chapter 4.2.



(a)



(b)

Fig.4.5 SEM images of aluminum oxide pattern. (a) top view

(b) cross section view of a-a'

4.2 Fabrication of radio-frequency (RF) antenna using local anodization

4.2.1 Introduction of RF patch antenna

Radio-frequency patch antenna was introduced by Howell in 1972 [49], which has two parallel metal sheets and form a resonant piece of micro-strip transmission line with a length of approximately one-half wavelength of the radio waves as shown in Fig. 4.6. The patch antenna has larger electrical performance than its physical dimensions. For this reason, it was adapted various micro devices in mobile navigation, DMB, and other portable machines. Many researchers proposed various design of patch antenna which transmits and receives at the GHz frequency [23], and generally, the performance was estimated by radiation pattern, antenna gain, polarization, impedance bandwidth, far-field radiation pattern, and so on. Among other things, reflection/return loss (S_{11}) is the most basic characteristic of the antenna performance. Others are determined and designed depending on the purpose of use.

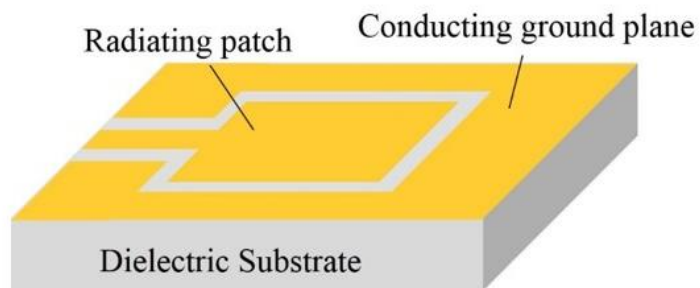
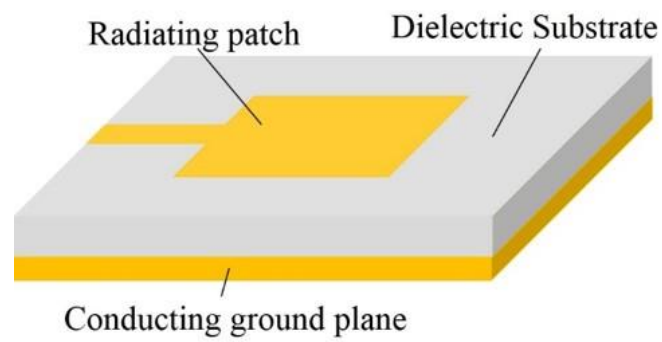


Fig. 4.6 Basic features of a patch and CPW patch antenna

Reflection loss is the loss of power in the signal reflected by a discontinuity in a transmission line or optical fiber [50]. If the power incident on the antenna-under-test is P_{in} and the power reflected back to the source is P_{ref} , the degree of mismatch between the incident and reflected power in the travelling waves is given by ratio P_{in}/P_{ref} . the higher this power ratio, is the better the load and line are matched[50]. Reflection loss (S_{11}) is defined as

$$RL = 10 \log \left(\frac{P_{in}}{P_{ref}} \right) \text{ dB} \quad (4.2)$$

which is a negative quantity, because general P_{ref} is larger than P_{in} . In this dissertation, by measuring the reflection loss of the fabricated patch antenna, the capability of penetrating oxide line pattern as an electric circuit was presented.

4.2.2 Fabrication of coplanar waveguide patch antenna

Coplanar waveguide (CPW) patch antenna is an alternative solution for feeding microstrip antennas which side-plane conductor is ground and center strip carries the signal [51]. Several shapes of the excitation slot have already been proposed by different authors. In CPW antennas, the metallic plane is used both as a conducting plane for the CPW line and a reflector plane for the radiating element. Although it has low volume, light weight and high performance, there are some challenges of narrow bandwidth and low signal gain caused by base substrate materials and its planar structure. To overcome these problems, air (cavity)-backed antenna (remove substrates material between radiating patch and ground plane) have been suggested in many studies [52-54]. However, the air space need to be supported by additional parts, it has limitations in terms of antenna miniaturization by MEMS process. In this case, local anodization can be the alternative fabrication method for the air-backed antenna. In the fabrication of aluminum electric circuit using local anodization, there are no need for base materials. Also fabricated aluminum sheet can act as a good conductor and insulator itself with structural stability. the geometrical configuration of the antenna was designed as a simple X-band antenna (which has 11 GHz resonance frequency) using the electromagnetic (EM) simulation. An aluminum oxide line was fabricated along the boundary of radiating

patch on a 10 μm -thick rectangular (6 mm x 10.5 mm) aluminum foil by local anodization. The fabricated CPW micro patch antenna was attached to a subminiature A-connector to measure the reflection loss (S11), which is the loss of power in the signal reflected by a discontinuity in a transmission line. The reflection loss was measured by a PNA Network Analyzer (E8364B, Agilent Technology) which has a testing range between 10 MHz and 50 GHz. Fig. 15 presents the reflection loss of the fabricated CPW patch antenna. A strong resonance occurred at 11.83 GHz and the reflection loss at this frequency was -35.4 dB. Generally, in terms of the evaluation of RF performance, micro patch antenna is required to have below -10 dB absorption.[49] From the results above, it can be concluded that local anodization can be used for the fabrication of a micro-electric circuit such as a micro-CPW antenna. Detailed anodization conditions are equal to that of fabrication of the penetrating oxide pattern.

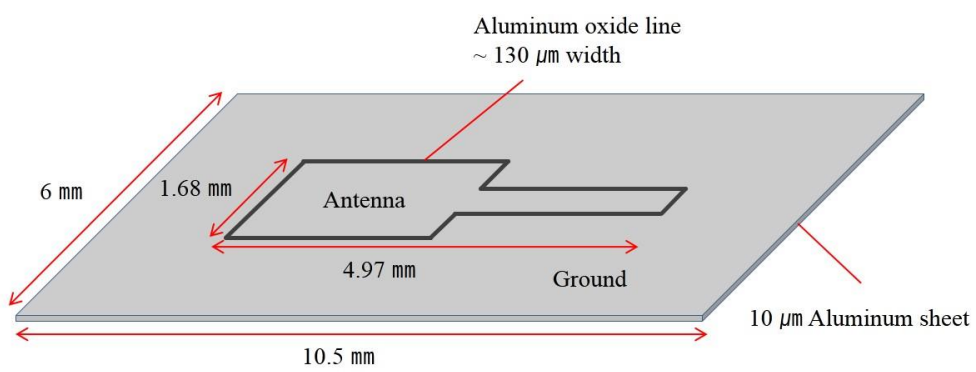


Fig.4.7 The geometrical configuration of the CPW micro patch antenna on aluminum sheet.

As shown in Fig.4.8, fabricated CPW patch antenna using local anodization was attached on the measuring subminiature version A (SMA) connector which is semi-precision coaxial RF connector developed for minimal antenna and for use DC to 18 GHz. The reflection coefficient, S_{11} , was measured by PNA Network Analyzer (E8364B, Agilent Technology) which has testing range between 10 MHz and 50GHz.

Fig.4.9 presents the reflection loss of the proposed CPW patch antenna. A strong resonance occurred at 11.83 GHz and the reflection loss at this frequency was – 35.4 dB. Generally, in the estimation of RF antenna performance, below -10 dB absorption is known for the suitable antenna [51]. Thus, it is confirmed that the local anodization can be used for fabrication of micro electric circuit like a micro CPW antenna.

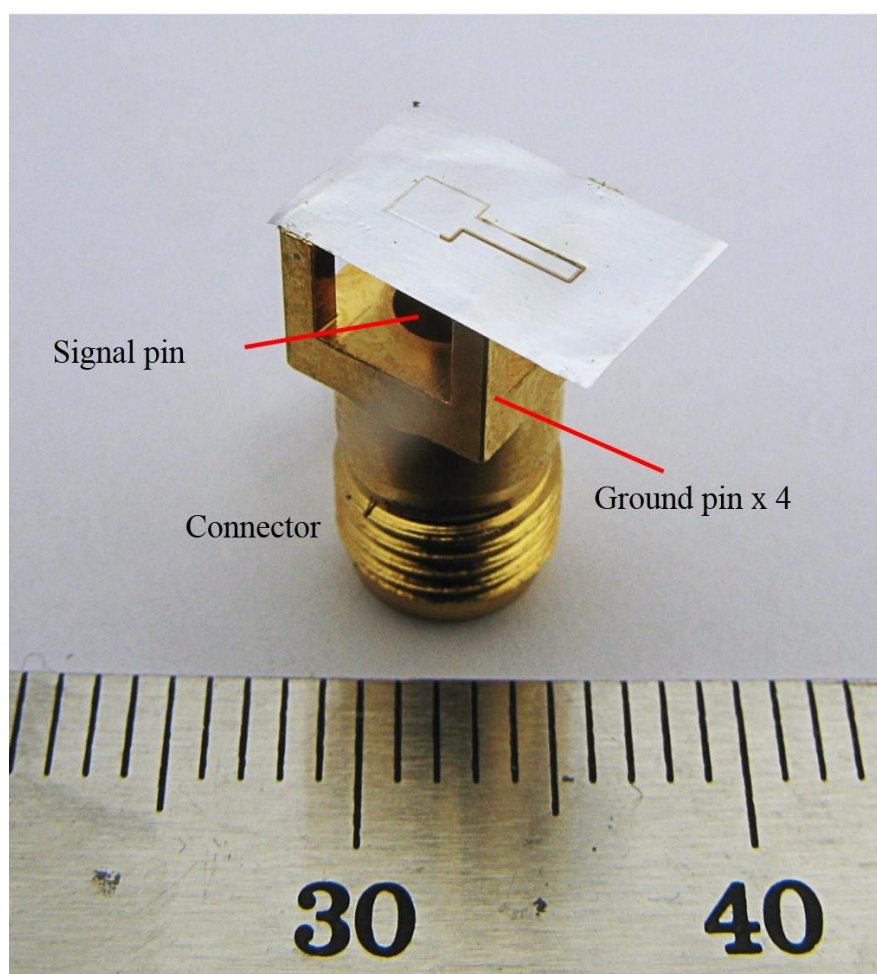


Fig.4.8 The fabricated CPW patch antenna using local anodization and was attached on the SMA connector.

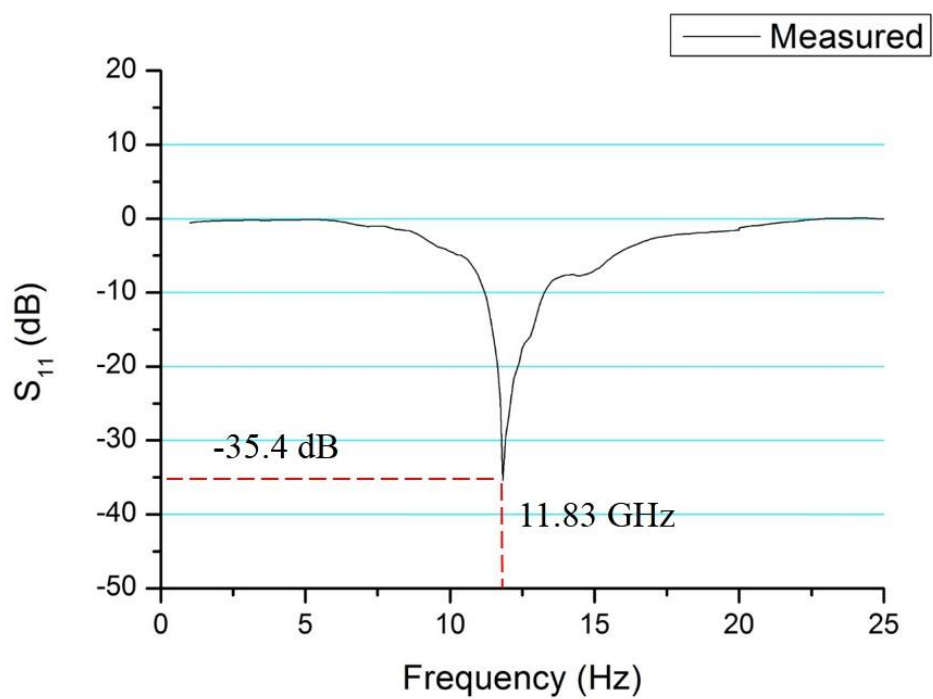
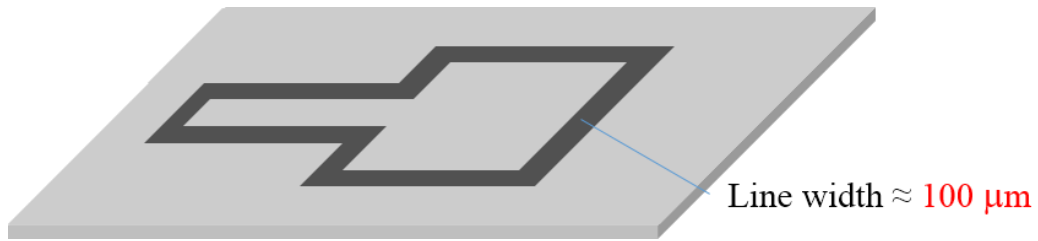


Fig.4.9 The absorbing performance of the fabricated CPW patch antenna

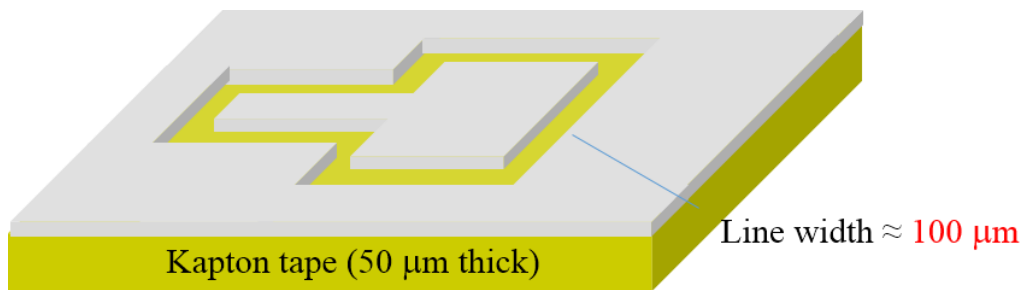
To prove why the local anodization is preferable on fabricating air-backed CPW patch antenna, effect of base material on CPW patch antenna was verified. As shown in Fig. 10, proposed antenna and same design with polyimide substrate (50 μm Kapton tape, DuPont™) were compared. As RF performance changes due to polyimide substrate, improved design was also compared. Antenna on polyimide substrate was machined by an ytterbium pulsed fiber laser (IPG photonics, YLP-C series). This pulsed fiber laser module provide a pulsed output beam with an average power that ranges from 2 W to 20 W and a pulse width of 100 ns. The wavelength is 1064 nm. The maximum pulse energy per pulse is 1 mJ at a pulse repetition rate of 20 kHz. Table 4.2 shows the laser beam conditions in fabrication of antenna. After the aluminum was machined, 50 μm thickness Kapton tape was attached under the aluminum sheet. Fabricated CPW antenna with polyimide base material is shown in Fig. 4. 11.

Parameters	Condition	Parameters	Condition
Average power	4 W	Repetition rate	80 kHz
Marking speed	19.6 mm/s	Repetition number	10 times

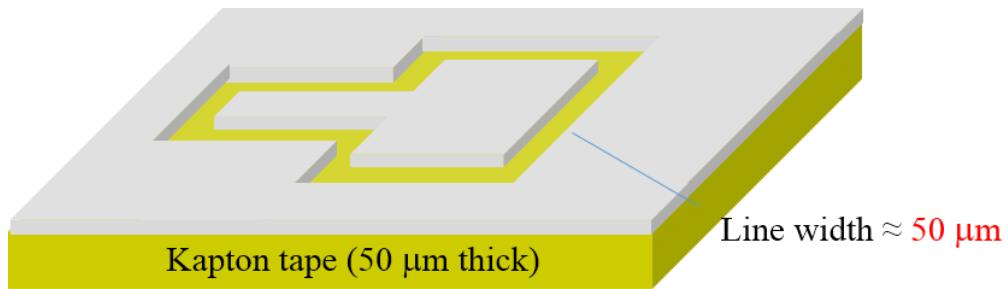
Table 4. 2 Conditions of laser beam machining process



(a) Original design (fabricated by local anodization)



(b) Original design + base material (fabricated by LBM)



(c) Improved design (fabricated by LBM)

Fig.4. 10 The geometrical configurations of air-backed antenna and antenna on polyimid substrate

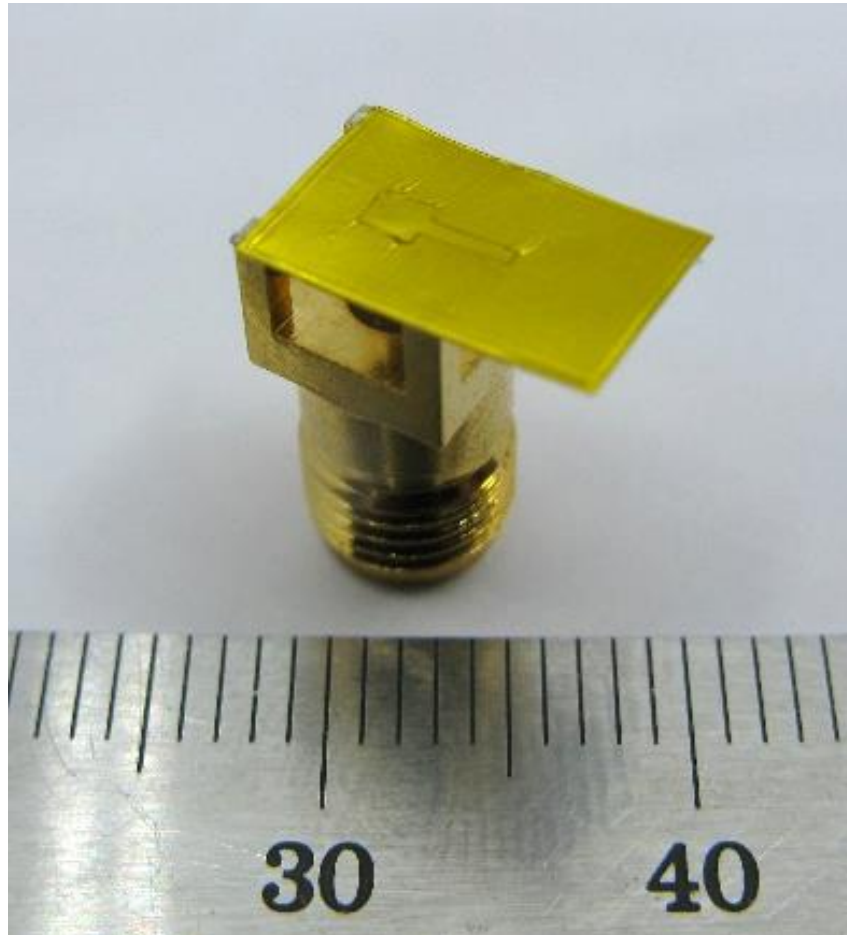


Fig.4. 11 The fabricated CPW patch antenna with polyimide substrates by LBM and was attached on the SMA connector

In the comparison of performance between each antennas shown in the Fig. 4. 12. Same design with polyimide substrate antenna has -17.01 dB reflection loss at the 10.79 GHz resonant frequency and its -10 dB-bandwidth is 1.237 dB. Its performance is worse than that of original antenna by local anodization. It is because the polyimide substrate, and the changed optimum RF characteristic effected by substrate. Thus it need to be improved. During the EM simulation, there was difficulty to improve both reflection loss and bandwidth at the same time. Blue line as shown in the Fig. 4.12, bandwidth increased to 1.237, but reflection loss decreased to -17.01 dB. As a results, it was verified that the local anodization is preferable on fabricating air-backed CPW patch antenna. Besides, compared with other single patch antenna with similar resonance frequency, it has small size and antenna performance. Generally, the patch size of the antenna is more than twice that of the proposed antenna [54-56].

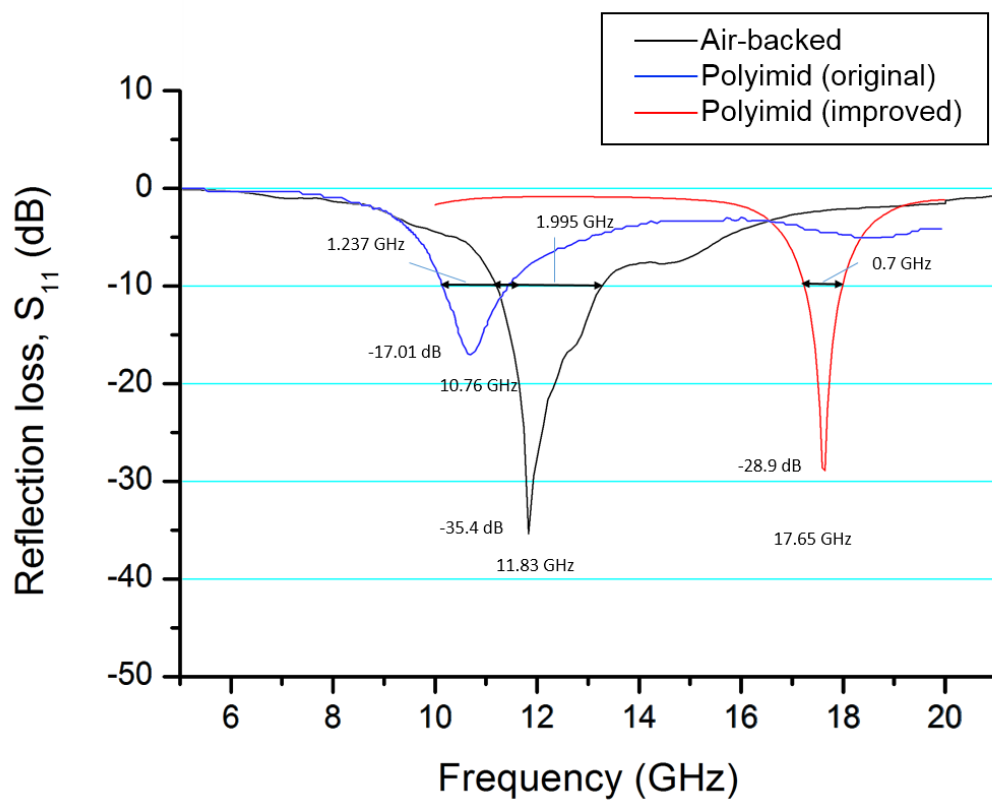


Fig.4. 12 Comparison of performance with reflection loss (S_{11}) and bandwidth (-10 dB)

4.2.3 Local anodization on the non-flat aluminum surface

Using local anodization technique, it is possible to fabricate the electric circuit not only on the flat surface, but also on the non-flat surface. When the inter-electrode gap is maintained and without geometric interference in tool path, local anodization can be used for every curved surface. As introduced in chapter 1, the remaining anodized oxide line will act as not only a dielectric material, but also a support of the structure. In this chapter, local anodization on the cylindrical aluminum surface was presented. However, suitable aluminum pipe which have thickness of 10 μm or less than 100 μm was hard to find and fabricate. Instead, flexible 10 μm thick aluminum sheet was wound on base aluminum shaft and local anodization is carried out on that surface. After the process, the base shaft was extracted. Curved oxide pattern structure was fixed to stand by itself.

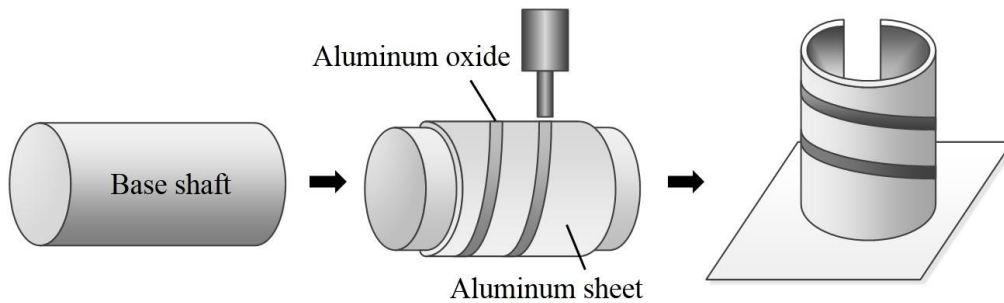
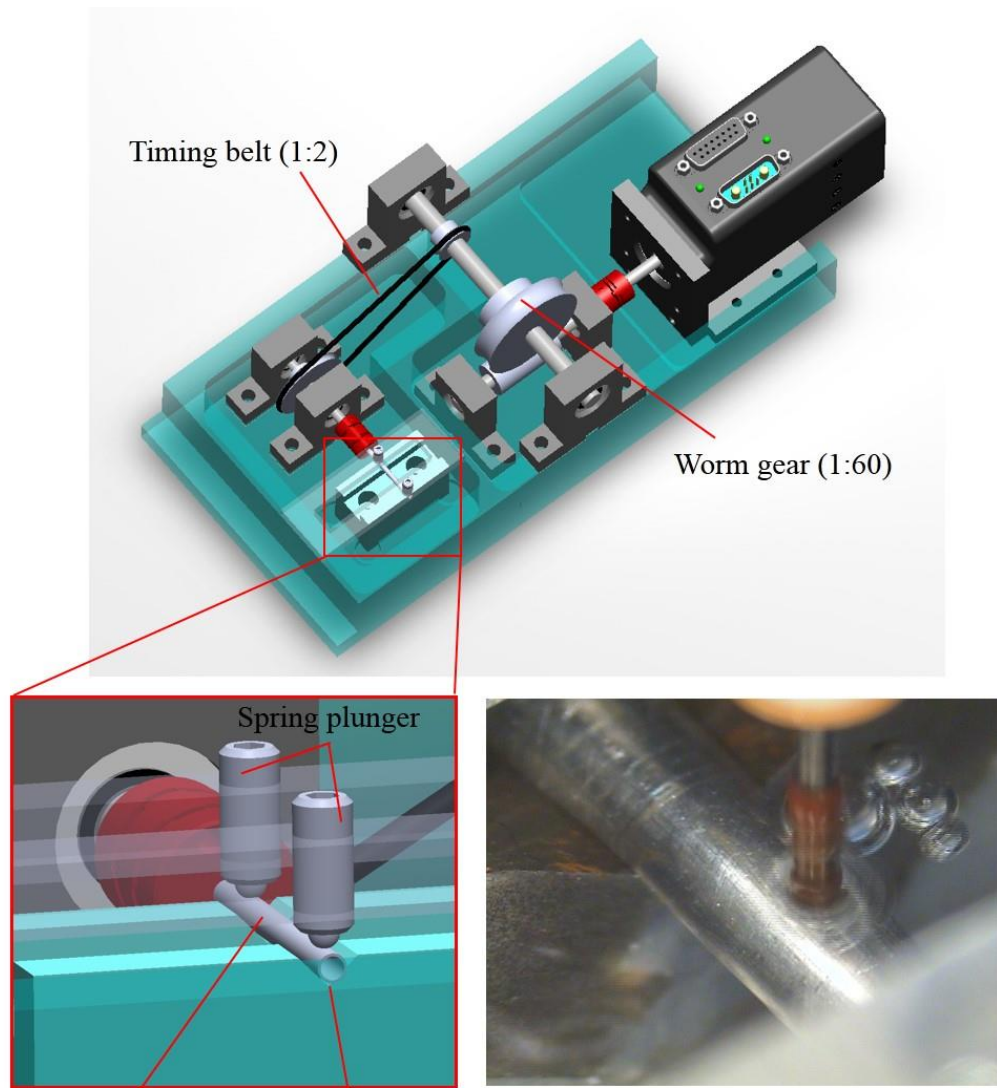


Fig.4.13 Local anodization process on the curved surface

To maintaining the inter-electrode gap and feed rate, new system for the rotation of the cylindrical workpiece. Fig. 4.13 shows the schematic of the rotation system. The electrolyte bath and gear systems are separated and minimize the run-out of the workpiece by using nonconductive V-groove and spring plungers. Rotation of workpiece was driven by servo motor (Smart Motor-SM17205D, Animatics Corporation) which includes a controller, an amplifier and an encoder. When the diameter of the surface is 2 mm, tool electrode travels about 6,283 μm per cycle. To set the feed rate to 1 $\mu\text{m}/\text{s}$, worm gear and timing belt are used. Other anodizing conditions are equal to that of fabrication of the penetrating oxide pattern and detailed conditions are presented in Table. 4.3. As shown in Fig.4.15, the micro oxide line pattern was fabricated on 2 mm diameter cylindrical surface. The pattern size is 600 μm x 600 μm , and the line width is about 120 μm .

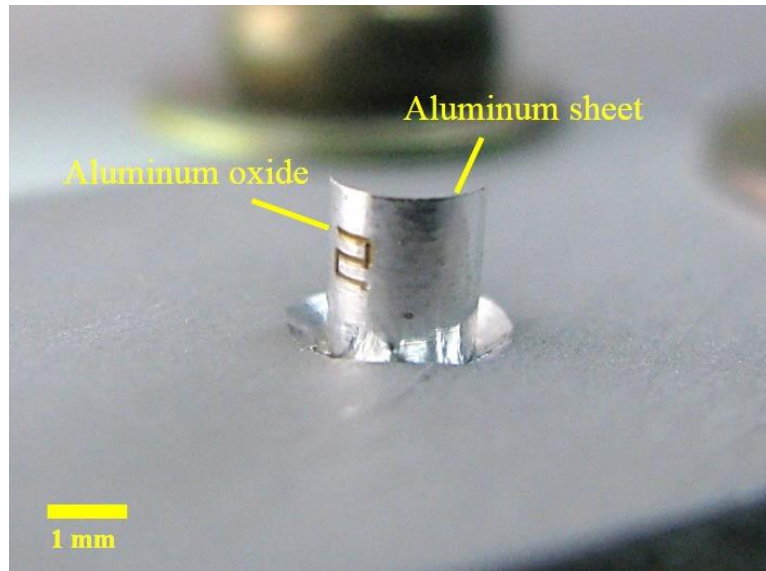


Workpiece (Al tube) V-groove

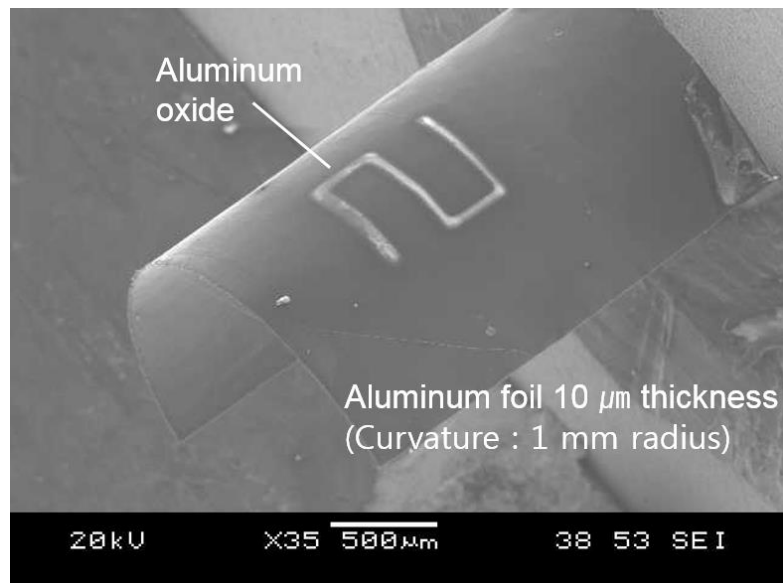
Fig.4.14 Schematic of the rotation system for local anodization on curved surface and image of fabrication

Parameters	Condition	Parameters	Condition
Workpiece	10 μm sheet, 99.999 % Aluminum	Electrolyte	0.5 M H_2SO_4 + 0.5 M H_2SO_4 = 1 : 3
Tool diameter	60 μm	Feed rate	1 $\mu\text{m}/\text{s}$
Pulse on time	0.5 μs	Pulse period	5 μs
Applied voltage	20 V	Inter-electrode gap	10 μm
Total gear ratio	1:120	Base shaft	\varnothing 2 mm–aluminum

Table 4.3 Conditions of local anodization for oxide pattern on curved surface



(a)



(b)

Fig.4.15 Optical and SEM image of aluminum oxide pattern on non-flat surface

Chapter 5

Conclusion

The 3D micro machining technology has become an important issue in the fabrication of micro parts or micro devices. Especially in the field of GHz RF antenna, as the size of the antenna has been decreased, performance of the antenna is very sensitive to base materials. The demands for guaranteeing durability, mobility have also increased. Local anodization is one of technologies which are suitable for the micro electric circuit. Anodized aluminum oxide is a good insulator and the process is very simple and can be applied to non-flat surface. Furthermore, remaining oxide layer by within the structure can support 3D structure.

In this work, local anodization process for fabrication of micro electric circuit was introduced. With ultra-short pulses, electrochemical reaction could be restricted to the vicinity of the electrode. Because local anodization is very sensitive to electrolyte property and voltage, it is very important to select proper electrolyte and

its concentration. Mixtures of sulfuric/oxalic acid electrolyte was tested as feasible electrolytes for aluminum. Behavior of localized oxide growth in different inter-electrode gap was analyzed using by field emission scanning electron microscopy (FE-SEM) including energy dispersive spectroscopy (EDS) and it was confirmed that the number of micro-depth localized aluminum oxide was fabricated at specific location on aluminum surface. Depth and width of the anodized oxide line were investigated in different ratios of sulfuric and oxalic acid mixtures at various microsecond pulse duration and applied voltage condition.

Based on the parameter test, the penetrating oxide line pattern was fabricated and verified its possibility as an electric circuit. Micro CPW patch antenna was fabricated by local anodization. The performance of the fabricated patch antenna was measured. A strong resonance occurred at 11.83 GHz and reflection loss at this frequency was -35.4 dB. In the estimation of general antenna performance, having below -10 dB absorption is known for the suitable antenna. Therefore, micro electric circuit was successfully fabricated by local anodization. Local anodization was also applied to non-flat cylindrical surface.

As a result, using the local anodization, fabrication of 3D micro electric circuit can be fabricated. Fabrication of 3D micro electric circuit using local anodization in more sophisticated system is expected.

References

1. Thompson, G.E., et al., *Anodic-Oxidation of Aluminum*. Philosophical Magazine B-Physics of Condensed Matter Statistical Mechanics Electronic Optical and Magnetic Properties, 1987. **55**(6): p. 651-667.
2. Ross, S.D., M. Finkelstein, and E.J. Rudd, *Anodic oxidation*. Organic chemistry, a series of monographs. 1975, New York: Academic Press. x, 339 p.
3. Henley, V.F., *Anodic oxidation of aluminium and its alloys*. 1st ed. The Pergamon materials engineering practice series. 1982, Oxford ; New York: Pergamon Press. x, 170 p.
4. G. C. Wood and J.P. O'sullivan, *The anodizing of aluminium in sulphate solutions*. *Electrochimica Acta*, 1970. **15**: p. 1865-1876.
5. Nicklen, D.A.L. and D.R. Gabe, *Ac Anodizing of Aluminum in Sulfuric-Acid*. *Surface Technology*, 1978. **7**(5): p. 353-359.
6. John, S., V. Balasubramanian, and B.A. Sheno, *Studies on Anodizing of Aluminum in Alkaline Electrolyte Using Alternating-Current*. *Surface Technology*, 1985. **26**(3): p. 207-216.
7. *ANODIC COATINGS FOR ALUMINUM AND ALUMINUM ALLOYS*, in *MILITARY SPECIFICATION*. 2003.
8. T., M., *State of the Art of Micromachining*. *Annals of the CIRP*, 2000. **49**(2): p. 473-488.
9. Kikuchi, T., et al., *Local surface modification of aluminum by laser irradiation*. *Electrochimica Acta*, 2001. **47**(1-2): p. 225-234.
10. Kikuchi, T., et al., *Fabrication of nickel micro-pattern on insulating board by anodizing/laser irradiation/electrodeposition*. *Surface & Coatings Technology*, 2003. **169**: p. 199-202.

11. Akiyama, Y., et al., *Local deposition of polypyrrole on aluminum by anodizing, laser irradiation, and electrolytic polymerization and its application to the fabrication of micro-actuators*. *Electrochimica Acta*, 2006. **51**(23): p. 4834-4840.
12. Shimizu, K., et al., *Structural Ordering in Annealed Anodic Oxide-Films on Aluminum*. *Philosophical Magazine Letters*, 1990. **61**(3): p. 133-137.
13. Li, F.Y., L. Zhang, and R.M. Metzger, *On the growth of highly ordered pores in anodized aluminum oxide*. *Chemistry of Materials*, 1998. **10**(9): p. 2470-2480.
14. Montero-Moreno, J.M., M. Sarret, and C. Muller, *Influence of the aluminum surface on the final results of a two-step anodizing*. *Surface & Coatings Technology*, 2007. **201**(14): p. 6352-6357.
15. Montero-Moreno, J.M., M. Sarret, and C. Muller, *Some considerations on the influence of voltage in potentiostatic two-step anodizing of AA1050*. *Journal of the Electrochemical Society*, 2007. **154**(3): p. C169-C174.
16. Cheng, H.C., et al., *Influence of hydrogen charging on the formation of nanostructural titania by anodizing with cathodic pretreatment*. *Journal of the Electrochemical Society*, 2007. **154**(1): p. E13-E18.
17. Marzocchi, V., et al., *The influence of tartaric acid additions on the anodizing behaviour of AA2024-T3 alloy in sulphuric acid*. *Corrosion Reviews*, 2007. **25**(3-4): p. 461-473.
18. Lee, W., et al., *Structural engineering of nanoporous anodic aluminium oxide by pulse anodization of aluminium*. *Nature Nanotechnology*, 2008. **3**(4): p. 234-239.
19. Gaston-Garcia, B., et al., *Local Burning Phenomena in Sulfuric Acid Anodizing: Analysis of Porous Anodic Alumina Layers on AA1050*. *Electrochemical and Solid State Letters*, 2010. **13**(11): p. C33-C35.
20. Gordon, A.E., et al., *Mechanisms of surface anodization produced by scanning probe microscopes*. *Journal of Vacuum Science & Technology B*, 1995. **13**(6): p. 2805-2808.
21. Dagata, J.A., et al., *Understanding scanned probe oxidation of silicon*. *Applied Physics Letters*, 1998. **73**(2): p. 271-273.

22. Liu, C.R., et al., *60-GHz LTCC Integrated Circularly Polarized Helical Antenna Array*. Ieee Transactions on Antennas and Propagation, 2012. **60**(3): p. 1329-1335.
23. Sumant, P.S., N.R. Aluru, and A.C. Cangellaris, *A Compact Model For Dielectric Charging in RF MEMS Capacitive Switches*. International Journal of Rf and Microwave Computer-Aided Engineering, 2009. **19**(2): p. 197-203.
24. Fakharzadeh, M., et al., *CMOS Phased Array Transceiver Technology for 60 GHz Wireless Applications*. Ieee Transactions on Antennas and Propagation, 2010. **58**(4): p. 1093-1104.
25. Enayati, A., et al., *3D-Antenna-in-Package Solution for Microwave Wireless Sensor Network Nodes*. Ieee Transactions on Antennas and Propagation, 2011. **59**(10): p. 3617-3623.
26. Rashed, A.N.Z. and H.A. Sharshar, *Optical microstrip patch antennas design and analysis*. Optik, 2013. **124**(20): p. 4331-4335.
27. Singh, T., *Design and finite element modeling of series-shunt configuration based RF MEMS switch for high isolation operation in K-Ka band*. Journal of Computational Electronics, 2015. **14**(1): p. 167-179.
28. Park, J., et al., *Fabrication of Aluminum/Alumina Patterns using Localized Anodization of Aluminum*. International Journal of Precision Engineering and Manufacturing, 2012. **13**(5): p. 765-770.
29. Mott, N.F., *A theory of the formation of protective oxide films on metals*. Transactions of the Faraday Society, 1939. **35**(2): p. 1175-1177.
30. Mott, N.F., *The Theory of the Formation of Protective Oxide Films on Metals* .3. Transactions of the Faraday Society, 1947. **43**(7): p. 429-434.
31. Cabrera, N.a.M., N. F., *Theory of the oxidation of metals*. Reports on Progress in Physics, 1949. **12**: p. 163-184.
32. Stadelmann, T.O., *Antidot superlattices in InAs-GaSb double heterostructures: transport studies*. 2006, University College, Oxford.
33. Fromhold, A.T., *Metal Oxidation-Kinetics from the Viewpoint of a Physicist - the Microscopic Motion of Charged Defects through Oxides*. Langmuir, 1987. **3**(6): p. 886-896.

34. Takahashi, H., Nagayama, M. Akahori, H. and Kitahara A., *Electron-microscopy of Porous Anodic Oxide Films on Aluminum by Ultra-thin Sectioning Technique, Part I*. Journal of Electron Microscopy, 1973. **22**(2): p. 149-157.
35. Keller, F., Hunter, M.S. and Robinson, D.L., *Structural Features of Oxide Coatings on Aluminum*. Journal of the Electrochemical Society, 1953. **100**(9).
36. Ahn, S.H., et al., *Electro-chemical micro drilling using ultra short pulses*. Precision Engineering-Journal of the International Societies for Precision Engineering and Nanotechnology, 2004. **28**(2): p. 129-134.
37. Paik, W.K.a.P., S. M., *Electrochemisty: Science and Technology of electrode Processes*. 2001, Seoul: Cheongmoongak.
38. Chung, D.K., B.H. Kim, and C.N. Chu, *Micro electrical discharge milling using deionized water as a dielectric fluid*. Journal of Micromechanics and Microengineering, 2007. **17**(5): p. 867-874.
39. Park, J.W., et al., *Wire Electrical Discharge Machining of Carbon Nanofiber Mats for Field Emission*. International Journal of Precision Engineering and Manufacturing, 2012. **13**(4): p. 593-599.
40. Song, K.Y., et al., *Electrical discharge machining using a strip electrode*. Precision Engineering-Journal of the International Societies for Precision Engineering and Nanotechnology, 2013. **37**(3): p. 738-745.
41. Aerts, T., et al., *Influence of the anodizing temperature on the porosity and the mechanical properties of the porous anodic oxide film*. Surface & Coatings Technology, 2007. **201**(16-17): p. 7310-7317.
42. Wheeler, J.M., J.A. Curran, and S. Shrestha, *Microstructure and multi-scale mechanical behavior of hard anodized and plasma electrolytic oxidation (PEO) coatings on aluminum alloy 5052*. Surface & Coatings Technology, 2012. **207**: p. 480-488.
43. Yokoyama, K., et al., *Advantages of Pulse Anodizing*. Plating and Surface Finishing, 1982. **69**(7): p. 62-65.
44. Yoshimoto, M., et al., *Anodizing of aluminum in sulfuric acid and oxalic acid solutions with percarboxylic acid-based additive*. Journal of the Ceramic Society of Japan, 2012. **120**(1403): p. 276-279.

45. Okubo, K., Toba, D. and Sakura, Y., *Studies of High-temperature, High Speed Anodic Oxidation of Aluminum by Pulse Current with Negative Current Component*. Journal of the Metal Finishing Society of Japan, 1988: p. 512-516.
46. Okubo, K., Suyama, S. and Sakura, Y., *Studies of Microstructure of Anodic Oxide Films on Aluminum by Pulse Current with a Negative Component*. J. of Surface Finishing Soc. of Japan, 1989. **40**(12).
47. Kim, B.H., et al., *Micro electrochemical machining of 3D micro structure using dilute sulfuric acid*. Cirp Annals-Manufacturing Technology, 2005. **54**(1): p. 191-194.
48. Kim, B.H., et al., *Micro electrochemical milling*. Journal of Micromechanics and Microengineering, 2005. **15**(1): p. 124-129.
49. Howell, J.Q., *Microstrip Antennas*. IEEE International Symposium on Antennas and Propagation, Williamsburg Virginia, 1972: p. 177-180.
50. Bird, T.S., *Definition and Misuse of Return Loss*. Ieee Antennas and Propagation Magazine, 2009. **51**(2): p. 166-167.
51. Giauffret, L., Laheurte, J. M., and Papiernik, A., *Study of various shapes of the coupling slot in CPW-fed microstrip antennas*. Ieee Transactions on Antennas and Propagation, 1997. **45**(4): p. 642-647.
52. Hong, W.B., N. Behdad, and K. Sarabandi, *Size reduction of cavity-backed slot antennas*. Ieee Transactions on Antennas and Propagation, 2006. **54**(5): p. 1461-1466.
53. Sun, Z.W. and P. Fay, *High-gain, high-efficiency integrated cavity-backed dipole antenna at Ka-band*. Ieee Antennas and Wireless Propagation Letters, 2006. **5**: p. 459-462.
54. Komulainen, M., et al., *Embedded air cavity backed microstrip antenna on an LTCC substrate*. Journal of the European Ceramic Society, 2007. **27**(8-9): p. 2881-2885.
55. Wi, S.H., Y.S. Lee, and J.G. Yook, *Wideband microstrip patch antenna with U-shaped parasitic elements*. Ieee Transactions on Antennas and Propagation, 2007. **55**(4): p. 1196-1199.
56. Masa-Campos, J.L., et al., *Stacked Circular Patch Antenna with Dual Right/Left Hand Circular Polarization for Wideband Applications in X*

Band. Microwave and Optical Technology Letters, 2009. **51**(6): p. 1419-1424.

국문초록

본 논문에서는 아노다이징의 국부화 기술을 이용한 마이크로 알루미늄 산화막 패턴의 제작에 관하여 연구하였다. 이 기술은 국소 양극 산화, 혹은 탐침형 원자 현미경 리소그래피를 이용한 나노 표면 처리 기술이다. 그러나 이 기술에 의해 생성된 산화막의 두께는 수 나노에서 수십 나노에 불과하다. 초단 펄스를 이용한 미세전해가공에서는 전기이중층의 원리로 전해 가공영역을 수 마이크로로 국부화시켰다. 미세전해가공의 원리를 이용하면 마이크로 깊이의 산화막을 국부화시킬 수 있다. 본 논문에서는 다양한 톨 간극에서 황산과 옥살산의 혼합액을 전해 용액으로 사용하여 국부적인 산화막의 생성과정을 전계방출형 주사전자현미경으로 관찰하고 성분을 분석하였다. 그리고 수 마이크로 깊이의 산화막이 국부적으로 생성되는 것을 확인하였다. 황산과 옥살산의 혼합비율, 다양한 주기의 펄스, 전압에 따른 국부화 아노다이징 양상과 산화막의 깊이, 두께를 측정, 분석하였다. 이를 바탕으로 마이크로 크기의 알루미늄 산화막 패턴을 가공하였으며 특히

GHz 대역의 마이크로 패치 안테나를 제작하고 그 반사손실을 측정하여 성능을 평가하였다. 또한, 원통형 표면에 알루미늄 산화막 패턴을 가공하여 삼차원 마이크로 전기회로 제작의 기술적용 가능성을 제시하였다.

주요어: 아노다이징의 국부화 기술, 국소 산화, 탐침형 원자 현미경, 전해 가공, 산화 알루미늄, 라디오 주파수 안테나

학번: 2008-22894